



Adaptive mesh refinement and cycle jumps for phase-field fatigue fracture modeling

Adrien Jacon ^{a,b,*}, Benoit Prabel ^{b,**}, Gergely Molnár ^a, Joffrey Bluthé ^b, Anthony Gravouil ^a

^a Univ Lyon, INSA-Lyon, CNRS UMR5259, LaMCoS, F-69621, France

^b Université Paris-Saclay, CEA, Service d'Etudes Mécaniques et Thermiques, 91191, Gif-sur-Yvette, France

ARTICLE INFO

Keywords:

Fracture mechanics
Phase-field
Fatigue crack propagation
Adaptive mesh refinement
Cycle jump scheme

ABSTRACT

A phase-field approach was used in order to model the complex mechanisms of fatigue crack nucleation and growth. This popular method enables a flexible framework that recovers accurately expected crack patterns. However, it usually suffers from several efficiency drawbacks, such as the need for a very fine mesh, and the heavy computational cost associated with the cycle by cycle approach. For this reason, we put forward the coupling of adaptive mesh refinement and cycle jumps, to significantly accelerate computing time, at a given level of accuracy. Several numerical examples were studied to showcase the abilities of the proposed coupling and some qualitative numerical/experimental comparisons were made. In the end, the proposed coupling was able to recover non accelerated results with significant computing gains.

1. Introduction

In modern industry, fatigue fracture is the predominant mode of failure of industrial components. This phenomenon is usually taken into account by adding broad safety margins to the final designs. In this context, accurate and robust simulation of crack initiation and propagation is essential to lower manufacturing and maintenance costs, while ensuring safety and reliable designs.

Fatigue crack nucleation and growth are caused by cyclic loads, and are characterized by load levels that can be much lower than under monotonic conditions. There are two main fatigue regimes: oligocyclic fatigue occurs for high loadings and relatively few cycles, whereas polycyclic fatigue takes place for low loadings and a high number of cycles. In the case of the former, plastic deformation usually plays a role. Conversely, only marginal amounts of plastic dissipation appear for polycyclic fatigue. In this work an elastic framework was used, and the study was thus limited to polycyclic fatigue, also known as high-cycle fatigue.

Most approaches used to model high cycle fatigue crack propagation rely on empirical laws derived from the study of linear elastic fracture mechanics introduced by Griffith [1] and the definition of stress intensity factors (SIF), K in Irwin's work [2]. Paris [3] put forward the idea to set the SIF range over a cycle, ΔK as the driving force of fatigue crack propagation. When plotting the representation of this idea, he observed three material dependent domains of crack propagation illustrated in Fig. 1. On a logarithmic scale, we distinguish domains of (I) nucleation, (II) stable crack propagation regime, and (III) unstable failure. The linear regime observed in (II) can be used to describe simple cases of crack propagation very reliably. However these approaches suffer from their empirical nature. As they are defined on simple cases, we can expect less predictive results for multi-directional loadings or complex crack patterns. Furthermore, since they are based on linear elastic fracture mechanics, additional criteria must

* Corresponding author at: Univ Lyon, INSA-Lyon, CNRS UMR5259, LaMCoS, F-69621, France.

** Corresponding author.

E-mail addresses: adrien.jacon@cea.fr (A. Jacon), benoit.prabel@cea.fr (B. Prabel).

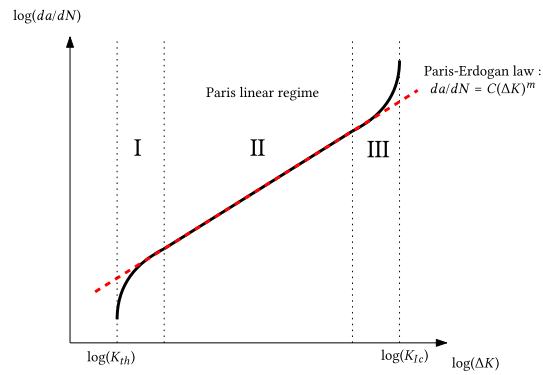


Fig. 1. A typical plot of crack growth rate as a function of the stress intensity range. The Paris-Erdogan equation displays a decent fit with the central linear section of regime II.

be setup to recover complex crack patterns. Additionally, crack initiation cannot be modeled and is therefore studied separately in a distinct branch of fatigue literature that employs its own set of empirical methods.

Recently, more flexible frameworks for studying fatigue crack propagation have been put forward in the literature. Those methods are supported by the phase-field approach for brittle fracture, which has recently gained significant popularity. The method is highly effective in handling complex crack cases and consistently replicates experimental observations in a unified manner. The phase-field framework for brittle fracture was based on Ref. [4] and introduced in Ref. [5], where Griffith's fundamental balance of energy is recast as a variational problem. Consequently, the crack position is recovered by simply solving a minimization problem. In order to capture the crack numerically, a diffuse representation is adopted such that the initial discrete crack is approximated by a damage field whose topology is controlled by a density function [5,6]. This diffuse representation is the key to the flexibility of the method in a finite element framework as it regularizes the discontinuity introduced by the crack. After numerous works applying phase-field to brittle fracture [7,8], some authors applied this framework to model fatigue crack propagation. At first, a term was added to the formulation in order to account for fatigue degradation, such as in Ref. [9], where a second phase-field variable is introduced, in Ref. [10], where a viscous term enables fatigue effects, or in Refs. [11,12], where dissipative terms lower the fracture threshold. However, most phase-field fatigue extensions rely on the modification of the damage energy to account for a measure of accumulated strain. These ideas were put forward in a phase-field framework first in Ref. [13] and extended to 2D/3D in Ref. [14]. A whole family of methods relying on this approach was thus born, e.g., Refs. [15–17], where the framework is extended to take ductile effects into account, or Simoes et al. [18] who put forward a shape memory alloy fatigue phase-field model, and Golahmar et al. [19] where hydrogen embrittlement is added to the formulation. Other works, such as Refs. [20–22], can be linked to this family of approaches because fatigue effects rely on the degradation of the toughness of the material. More recently, multiple authors have been setting a unified framework for such local toughness degradation approaches, such as Alessi et al. [23], where those approaches are compared and sound theoretical grounds are set, or Golahmar et al. [24] where multiple degradation functions and accumulation methods are introduced to model known fatigue effects. Following these references, the proposed implemented fatigue extension was inspired by the work of Carrara et al. [14].

These approaches have been shown to possess predictive capabilities in a fatigue context but accelerating tools are necessary to apply the framework on industrial cases [21]. Indeed, in the considered model, damage evolution is a multi-scale phenomenon, both in space and time. First, it affects the structure on multiple timescales. On the one hand, a component's lifetime can consist of as many as 10^7 cycles. However, understanding the changes operating at the scale of a single cycle is crucial and influences the behavior at the macroscale (i.e., the component's total lifetime). But, calculating every cycle in detail can result in excessively long computing times. In this context, we implemented an iterative cycle jump scheme inspired by Loew's work [25] to accelerate lifetime predictions significantly. Secondly, the model affects multiple scales of space. Indeed, in a framework of continuum mechanics, fatigue introduces a discontinuity in a very localized active process zone, and accurately capturing it is essential to predict the propagation mechanisms. In a finite element framework, this means that a very local area (compared to typical structure dimensions) has to be meshed very finely in order to reach convergence. However, as crack paths are unknown before-hand, large scale phase-field simulations cannot be viable without adaptive mesh refinement (AMR), i.e., refinement of the mesh during propagation, in the relevant zones. To this end, a hierarchical adaptive mesh refinement process working with the phase-field model was adopted.

Ultimately, to simultaneously consider the micro and macro scales in space and time while increasing computational efficiency, we propose combining adaptive mesh refinement and cycle jump techniques within a fatigue fracture phase-field framework. In this way, multiple efficiency issues of the phase-field model are treated all at once, enabling the use of the model on real-life fatigue fracture applications. Additionally, the proposed coupling aims at maintaining the versatility of the phase-field model, allowing it to accurately capture complex crack cases such as kinking, branching, coalescing, and nucleation. Moreover, even with the use of the proposed acceleration techniques, the solution's accuracy must be ensured.

The present paper has been structured as follows: the fatigue fracture phase-field model used herein is briefly introduced in Section 2. Then, the numerical implementation of the model, and the computation of a cycle is detailed in Section 3. Next, the two accelerating tools are introduced in Sections 4 and 5 respectively. Finally, Section 6 describes the numerical study of several 2D geometries, in order to illustrate the accuracy, robustness and efficiency of the new model.

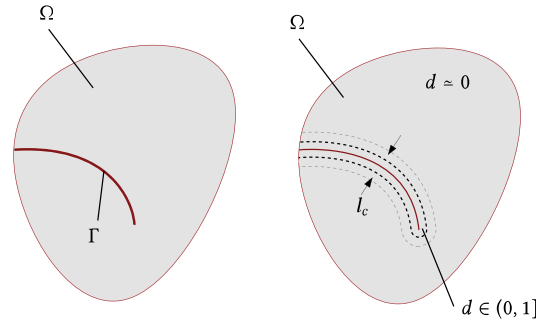


Fig. 2. The left image represents a cracked body with a discrete fracture, while the right one depicts the same scenario with the crack discontinuity regularized using the diffuse phase-field representation.

2. Phase-field fatigue model

2.1. Phase-field basics

Following the seminal work in Ref. [4], a functional can be set to reframe Griffith’s energy balance into a variational form:

$$\Pi_{int}^0(\mathbf{u}, \Gamma) = E_0(\mathbf{u}) + W_0(\Gamma) = \int_{\Omega} \psi_0 \, dV + \int_{\Gamma} G_c \, dS. \tag{1}$$

This is the internal energy of a cracked body. For instance, $E_0(\mathbf{u})$ is the mechanical component with ψ_0 the elastic energy density. W_0 is expressed as G_c , the critical fracture toughness of the material, integrated over the crack area Γ to represent energy dissipation in fracture.

A phase-field parameter d is introduced to regularize the crack surface, enabling a regularized formulation of functional (1) is obtained following Ref. [5]:

$$\Pi_{int}(\mathbf{u}, d) = E(\mathbf{u}, d) + W(d) = \int_{\Omega} g(d)\psi_0 \, dV + \int_{\Omega} G_c \cdot \left(\frac{d^2}{2l_c} + \frac{l_c |\nabla d|^2}{2} \right) \, dV. \tag{2a}$$

This regularized formulation can be seen as the free energy functional of the damage model. In such a setting, the phase-field parameter d represents damage. It ranges from 0 to 1, where 0 stands for the intact material while 1 stands for the fully broken one. It should be noted that it is defined on the whole domain Ω .

Additionally, $E(\mathbf{u}, d)$, the mechanical term, is now affected through d by a degradation function $g(d)$. As a result, when damage increases, the mechanical response is softened. A parabolic degradation function is used, and, as in the following Refs. [7,8] a small parameter k , is introduced to ensure the stability of the solution.

$$g(d) = (1 - d)^2 + k. \tag{3}$$

Finally, $W(d)$ still represents the energy of the crack, i.e., G_c integrated over the fracture surface, here defined as a surface functional. This functional approximates the discrete crack topology, with a surface density function smeared over the characteristic length l_c as is illustrated in Fig. 2. We can hence define the area of the crack as:

$$A(d) = W(d)/G_c = \int_{\Omega} \frac{d^2}{2l_c} + \frac{l_c |\nabla d|^2}{2} \, dV. \tag{4}$$

It makes for a very reliable damage global quantifier, and will therefore be used to evaluate precision in Section 6. Here, the crack area regularization is the same as in Ref. [7], and it is called the AT2 model. It enables automatic bounding of d between 0 and 1. However, it suffers from the lack of an elastic threshold. Indeed, any amount of loading triggers damage. To circumvent these limitations, multiple authors investigate other crack representation functions such as the AT1 model [26] or linear combinations of those functions [27].

The presented variational formulation is proved to Γ -converge, meaning that the functional (2a) minima and minimizers converge to the minima and minimizers of functional (1) as l_c approaches 0. In this sense, l_c is a regularization parameter of the linear elastic fracture mechanics variational problem. On the contrary, from a damage mechanics perspective, l_c drives the width of the diffused crack and is related to the tensile strength of the material. As such, it is linked to a material related property [28–30].

2.2. Crack growth in compression

Two mechanical energy $E(u, d)$ formulations have been implemented to reproduce different crack propagation phenomenologies. Firstly, an isotropic formulation is used:

$$E(\mathbf{u}, d) = \int_{\Omega} g(d) \cdot \psi_0 \, dV. \tag{5}$$

This formulation means that a structure degrades symmetrically with respect to tensile/compressive loadings. However, experimental observations support another phenomenology: crack propagation is driven differently based on the direction of the load with respect to crack directions. According to Refs. [7,31], the free energy density ψ_0 is thus decomposed into a positive part ψ^+ due to tension, and a negative part ψ^- due to compression, so as to reproduce this asymmetric behavior. This decomposition can be expressed by rewriting the mechanical energy term in functional (2a) as:

$$E(\mathbf{u}, d) = \int_{\Omega} g(d) \cdot \psi_0^+ + \psi_0^- dV. \quad (6)$$

Only the tensile part ψ_0^+ of the mechanical energy is degraded and drives the crack propagation. Additionally, in this fatigue extended formulation, it drives fatigue degradation. This work uses a spectral decomposition of the mechanical energy, and in this respect, it is the sign of the principal strains that discriminates between tensile and compressive terms. A detailed implementation of the chosen spectral decomposition is developed in Molnár et al. [26].

2.3. Fatigue effects

Fatigue damage originates from the accumulation of mechanical energy. To enable crack propagation below the monotonic threshold, G_c is degraded as a function of this cumulated term. Indeed, as in linear elastic fracture mechanics, G_c is a fracture threshold material parameter: degrading this parameter thereby enables crack propagation for loadings below the usual fracture threshold. Fatigue effects are thus reproduced phenomenologically, and we write:

$$G_F = f(\bar{\alpha}) \cdot G_c, \quad (7)$$

where $f(\bar{\alpha})$ is a fatigue degradation function, influenced by the cumulated variable $\bar{\alpha} \equiv \int_0^t \langle \dot{\alpha} \rangle^+ dt$, with $\langle X \rangle^+$ being the positive part of X . As advised in Ref. [14], we set $\alpha = g(d) \cdot \psi_0^+$, which means that the active part of elastic energy, degraded by $g(d)$ is cumulated. The degradation function is taken into account to stop the build-up of energy in the damaged zone. Moreover, we underline how this fatigue cumulated variable $\bar{\alpha}$ is computed. Thus, in a time discretized setting, at a given time-step n we use quantities computed at $n-1$ such that:

$$\bar{\alpha}_n = \bar{\alpha}_{n-1} + \int_{n-1}^n \langle \dot{\alpha} \rangle^+ dt, \quad (8a)$$

$$\simeq \bar{\alpha}_{n-1} + |\alpha_n - \alpha_{n-1}| \cdot \mathcal{H}(\alpha_n - \alpha_{n-1}), \quad (8b)$$

Here, \mathcal{H} is the Heavyside function that disables cumulative effects in unloading phases. This expression is in line with the work of Ref. [14] for a mean load independent model.

Multiple fatigue degradation functions have been put forward in the literature, set as functions varying between 1 and 0, remaining constant before a threshold of cumulated energy is reached, and being a strictly decreasing function. Following Ref. [14] we used two fatigue degradation functions, starting with a one parameter asymptotic degradation function, only driven by its threshold α_T :

$$f(\bar{\alpha}) = \begin{cases} 1 & \text{if } \bar{\alpha} < \alpha_T, \\ \left(\frac{2\alpha_T}{\bar{\alpha} + \alpha_T} \right)^2 & \text{if } \bar{\alpha} > \alpha_T. \end{cases} \quad (9)$$

Then, a second degradation function, also introduced in Ref. [14], was investigated as it is driven by two parameters, α_T and κ , a logarithmic degradation function.

$$f(\bar{\alpha}) = \begin{cases} 1 & \text{if } \bar{\alpha} < \alpha_T, \\ \left(1 - \kappa \log\left(\frac{\bar{\alpha}}{\alpha_T}\right) \right)^2 & \text{if } \alpha_T < \bar{\alpha} < \alpha_T 10^{1/\kappa}, \\ 0 & \text{if } \bar{\alpha} > \alpha_T 10^{1/\kappa}. \end{cases} \quad (10)$$

More informations on the construction and improvement of those two fatigue degradation functions can be found in Refs. [14,24].

With the given model, when a cyclic loading is applied to a structure, the first cycle triggers a very small damage increment. However, no damage localization can occur since the applied cyclic loading is very small compared to the usual critical loading in brittle fracture. This is valid until the cumulated variable reaches the specific threshold α_T , in which case, it triggers the degradation of G_F and enables crack propagation for very low cyclic loadings. This crack propagation can be considered as unstable, but it is confined to the zone where G_F is degraded. This way, tools derived from the variational approach for brittle fracture are used to model fatigue crack propagation.

The physical interpretation of this local degradation of the fracture toughness by the accumulation of elastic energy is however not straightforward. This elastic energy accumulation could be representative of the micro-structural effects leading to fatigue crack propagation. The interested reader can learn more about this type of phase-field fatigue model in Refs. [13,14,23]

2.4. Coupled problem statement

Let us now set a boundary value problem on domain Ω , with the domain boundary $\partial\Omega = \partial\Omega_t \cup \partial\Omega_u$. Here, $\partial\Omega_t$ is linked to Neumann boundary conditions, and $\partial\Omega_u$ to Dirichlet boundary conditions. We introduce the external potential:

$$\Pi_{ext}(\mathbf{u}) = \int_{\Omega} \mathbf{b} \cdot \mathbf{u} dV + \int_{\partial\Omega_t} \mathbf{t} \cdot \mathbf{u} dS, \quad (11)$$

where \mathbf{b} and \mathbf{t} are the external volume and boundary forces respectively. In a quasi-static setting we set the Lagrangian of this coupled problem to:

$$\mathcal{L}(\mathbf{u}, d) = \Pi_{int}(\mathbf{u}, d) - \Pi_{ext}(\mathbf{u}). \quad (12)$$

To solve the coupled problem we study the variation of the Lagrangian as:

$$\delta\mathcal{L} = \delta\Pi_{int} - \delta\Pi_{ext} = 0. \quad (13)$$

First, we derive the variation of internal energy:

$$\delta\Pi_{int} = \frac{\partial\Pi_{int}}{\partial\boldsymbol{\varepsilon}} \delta\boldsymbol{\varepsilon} + \frac{\partial\Pi_{int}}{\partial d} \delta d = 0, \quad (14a)$$

$$= \int_{\Omega} \left(g(d) \frac{\partial\psi_0^+}{\partial\boldsymbol{\varepsilon}} + \frac{\partial\psi_0^-}{\partial\boldsymbol{\varepsilon}} \right) \delta\boldsymbol{\varepsilon} dV + \int_{\Omega} \left(\frac{\partial g(d)}{\partial d} \psi_0^+ + \frac{G_F}{l_c} d \right) \delta d + (G_F l_c \nabla d \cdot \nabla \delta d) dV. \quad (14b)$$

Note that small perturbations are assumed, such that displacements are small and the strain tensor is linear: $\boldsymbol{\varepsilon} = \frac{1}{2} (\nabla\mathbf{u} + \nabla\mathbf{u}^T)$. The symmetric Cauchy stress tensor appears in expression (14b) as:

$$\boldsymbol{\sigma} = g(d) \frac{\partial\psi_0^+}{\partial\boldsymbol{\varepsilon}} + \frac{\partial\psi_0^-}{\partial\boldsymbol{\varepsilon}}. \quad (15)$$

Next, we write the variation of the external potential as:

$$\delta\Pi_{ext} = \int_{\Omega} \mathbf{b} \cdot \delta\mathbf{u} dV + \int_{\partial\Omega_t} \mathbf{t} \cdot \delta\mathbf{u} dS. \quad (16)$$

Applying the divergence theorem to Eq. (13), where we injected Eq. (14b) and (16), and factorizing out $\delta\mathbf{u}$, δd , yields the following strong form equation system of the coupled mechanical and phase-field problem:

$$\nabla\boldsymbol{\sigma} - \mathbf{b} = 0 \text{ on } \Omega, \quad (17a)$$

$$\boldsymbol{\sigma} \cdot \mathbf{n} = \mathbf{t} \text{ on } \partial\Omega_t, \quad (17b)$$

$$\mathbf{u} = \hat{\mathbf{u}} \text{ on } \partial\Omega_u, \quad (17c)$$

$$\frac{G_F}{l_c} d - G_F l_c \Delta d + 2(1-d)\psi_0^+ + \nabla f(\bar{\alpha}) \cdot \nabla d = 0 \text{ on } \Omega, \quad (17d)$$

$$\nabla d \cdot \mathbf{n} = 0 \text{ on } \partial\Omega_d. \quad (17e)$$

Solving the presented system in a monolithic manner can display convergence issues in the case of unstable crack propagation. Consequently, Miehe et al. proposed a staggered approach to solve this system for \mathbf{u} and d [7]. This approach is very robust, even in cases of unstable propagation. However, global convergence still needs to be verified to ensure that the precision is independent of the time step. Alternatively, a very fine time-step should be applied [8]. In the present work, a staggered approach was chosen for its robustness and ease of implementation. A detailed explanation of this staggered implementation is provided in Section 3.

2.5. Damage irreversibility

Staggered phase-field models, enable the use of a specific method to enforce irreversibility [7]. In this framework, the authors replaced ψ_0^+ in Eq. (17d) i.e., the mechanical contribution “seen” by the phase-field problem, with a history field H . This newly introduced field is defined as the maximum value of ψ_0^+ over the computed time interval whose continuous and discretized expressions are:

$$H(t) = \max_{\tau \in [0:t]} (\psi_0^+(\tau)) \quad (18a)$$

$$H_{n+1} = \begin{cases} \psi_0^+(\epsilon) & \text{if } \psi_0^+(\epsilon) > H_n, \\ H_n & \text{otherwise,} \end{cases} \quad (18b)$$

where H_n is the history-field computed at the previous step. This formulation enables H to satisfy the Karush–Kuhn–Tucker condition:

$$\psi_0 - H \leq 0, \quad \dot{H} \geq 0, \quad \dot{H}(\psi_0 - H) = 0, \quad (19)$$

in loading and unloading, signifying that the driving force of fracture cannot decrease: a damaged zone will not recover even in unloading scenarios. We can rewrite the equation of the damage problem (17d), as:

$$\frac{G_F}{l_c} d - G_F l_c \Delta d + 2(1-d)H + \nabla f(\bar{\alpha}) \cdot \nabla d = 0. \quad (20)$$

3. Staggered algorithm for the computation of one cycle

The presented coupled problem was solved in a staggered manner, following Refs. [5,7]. In other words, two sub-problems were set-up. First a mechanical problem (17a), (17b), (17c) was solved, then a damage problem (20), (17e). When minimizing the mechanical equations, the damage was kept constant, whereas in the case of the phase-field problem, the formerly determined elastic energy is employed. In this section, we describe such a fatigue phase-field staggered algorithm. Furthermore, the corresponding finite element implementation of both sub-problems is detailed in Appendix.

It should be noted that all numerical strategies mentioned in this article were implemented on the finite element software Cast3M [32]. There have been multiple usages of this software to study fracture mechanics such as in Helfer et al. [33], Lu et al. [34], and Riad et al. [35] where a phase-field model for brittle fracture was implemented. Also, in Gibert et al. [36] an adaptive mesh refinement strategy was applied in an eXtended Finite Element Method (XFEM).

A full cycle is computed as follows: n_{\max} time steps per cycle are computed, and at each time step n , a global convergence loop is set up where i indicates the iteration index.

- First, a mechanical problem influenced by constant damage is solved to find $\mathbf{u}_n^i = \mathbf{u}_{n-1} + \Delta \mathbf{u}_n^i$
- Then, fatigue cumulated energy is computed with Eq. (8) giving $\bar{\alpha}_n^i$, and G_F^i
- Finally, a damage problem influenced by the current $\bar{\alpha}_n^i$ and \mathbf{u}_n^i (through H_n^i) is solved for \mathbf{d}_n^i

Global convergence is then verified through the convergence of the dissipated energy expressed as $W(d)$, defined in Eq. (2a). We chose to normalize the criterion by the current value of dissipated energy $W^i(d)$. The convergence criterion can be written as:

$$W(d)^i - W(d)^{i-1} < W(d)^i \cdot 10^{-6}. \quad (21)$$

This convergence check enables a precision that is independent of the number of used time steps per cycle, as long as the extrema of the cyclic loading are captured.

The described iterative process is detailed in Algorithm 1. It is very close to the staggered implementation proposed in Miehe et al. [7]. However, global convergence was checked, as originally proposed by Bourdin et al. in [5]. Other schemes have been tested in the literature such as Ref. [34] where multiple staggered minimization schemes are put forward or such as Ref. [37], where the uncoupled framework is solved using a BFGS quasi-Newton approach.

Algorithm 1 Cycle computation algorithm

```

1: for  $n = 1, n_{\max}$  do
Require:  $\mathbf{d}^{i-1} \leftarrow \mathbf{d}_{n-1}, \bar{\alpha}^{i-1} \leftarrow \bar{\alpha}_{n-1}, H^{i-1} \leftarrow H_{n-1}$ , note that  $\mathbf{u}^{i-1} \leftarrow \mathbf{0}$ 
2:   while Global convergence is not achieved do
3:     Mechanical problem: Computation of  $\mathbf{u}^i$  influenced by  $\mathbf{d}^{i-1}$  with iterative search (A.4)
4:     Irreversibility: Computation of  $H^i$  (18b)
5:     Fatigue: Computation of  $G_F^i$  influenced by  $\bar{\alpha}_i$  with Eqs. (8b) and (7)
6:     Damage problem: Computation of  $\mathbf{d}^i$  influenced by  $\mathbf{u}^i, \bar{\alpha}^i$  and  $H^i$ 
7:     Global convergence check:
8:     • Criterion on damage dissipation convergence Eq. (21)
9:     if Convergence is checked then
10:       Update  $\mathbf{d}_n \leftarrow \mathbf{d}^i, \bar{\alpha}_n \leftarrow \bar{\alpha}^i, H_n \leftarrow H^i$ 
11:       Next time step  $n + 1$  quit
12:     else
13:       Update  $\mathbf{d}^{i-1} \leftarrow \mathbf{d}^i$ 
14:       Restart computation of time step  $n$ 
15:     end if
16:   end while
17: end for

```

4. Cycle jump schemes

Cycle by cycle simulation of high cycle fatigue crack propagation is inefficient, because in an industrial setting, lifetime predictions can be as much as 10^5 to 10^7 cycles. To speed up the computation time, we propose incorporating cycle skipping techniques into the previously introduced framework.

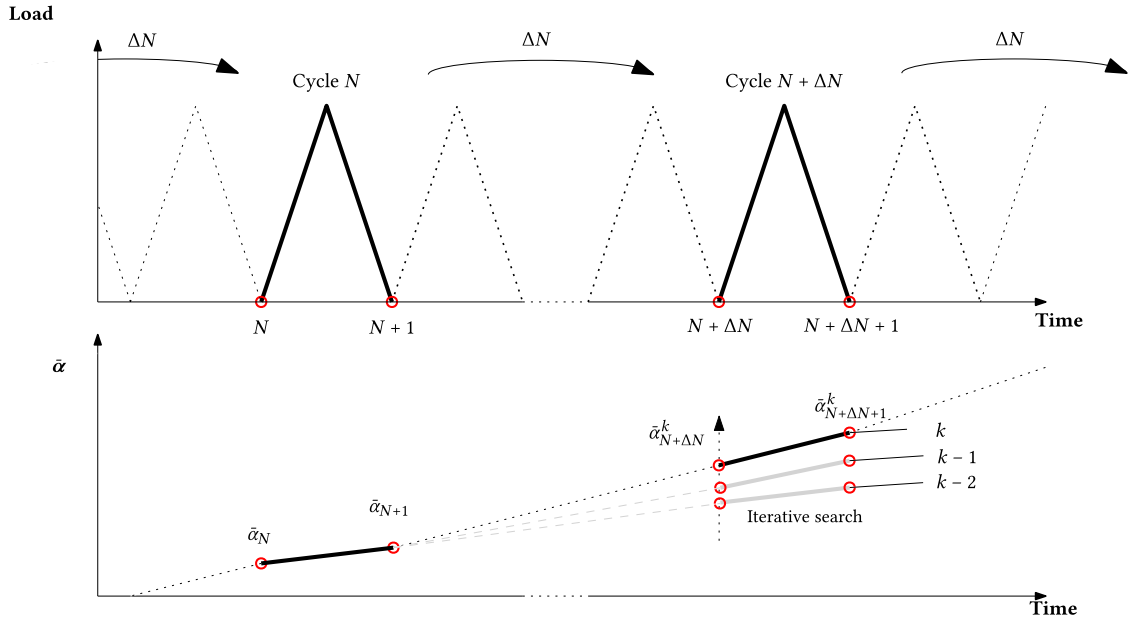


Fig. 3. Illustration of the iterative cycle jump scheme with two graphs. We first represent the cyclic loading, with the computed cycles in bold (upper figure) and then the evolution of $\bar{\alpha}$ with respect to the elapsed cycle (lower figure). Two control cycles are initially computed, after which iterative scheme is used to search for $\bar{\alpha}_{N+\Delta N}$, yielding a new control cycle.

Cycle skipping schemes rely on the idea of alternating between computation of cycles, and extrapolation of the time evolving quantities over ΔN cycles. Hence, the computation of ΔN cycles can be avoided. Computing cycles provide insight into the evolution of quantities through a process referred to as “control cycles”. Based on this information, a specific extrapolation method must be selected to maintain the accuracy of the solution.

This kind of technique was introduced in fatigue simulations in the very similar context of damage mechanics. We reference multiple authors using those cycle jump tools to accelerate fatigue simulations [38–40]. Furthermore, similar tools were recently applied to phase-field fracture [17,25,41]. The following section introduces a cycle-skipping scheme, inspired by the work in Ref. [25], adapted to the previously presented elastic fatigue framework.

4.1. Iterative cycle jump scheme

The extrapolation scheme was chosen to be implicit, meaning that we used information from one control cycle at N , before the cycle jump, and information from one control cycle at $N + \Delta N$, after the cycle jump. For this specific elastic framework, we extrapolate only $\bar{\alpha}$, the cumulated mechanical energy. This variable is ideal for the method as it evolves in a regular manner with respect to elapsed cycles, making a single control cycle representative of its general behavior. Additionally, $\bar{\alpha}$ cannot be computed back from the other fields as it depends on the loading history. Finally, in the elastic framework, every other field can be computed back from its value.

As stated in Ref. [25], we employed a trapezoidal extrapolation scheme that is based on the change in the current cycle (N) and the predicted cycle ($N + \Delta N$).

$$\bar{\alpha}_{N+\Delta N} = \bar{\alpha}_N + \frac{\Delta N}{2} (\dot{\bar{\alpha}}_N + \dot{\bar{\alpha}}_{N+\Delta N}) . \tag{22}$$

With the quantities represented in Fig. 3, we can define the terms of this expression as follows:

$$\dot{\bar{\alpha}}_N = \bar{\alpha}_{N+1} - \bar{\alpha}_N , \tag{23}$$

$$\dot{\bar{\alpha}}_{N+\Delta N} = \bar{\alpha}_{N+\Delta N+1} - \bar{\alpha}_{N+\Delta N} . \tag{24}$$

A Newton–Raphson scheme was implemented to search iteratively an extrapolated value of $\bar{\alpha}_{N+\Delta N}$ that enforces this trapezoidal extrapolation rule. Eq. (22) gives us the following cycle jump residual:

$$R_{cj} = \bar{\alpha}_N \cdot \left(1 - \frac{\Delta N}{2}\right) + (\bar{\alpha}_{N+\Delta N+1} + \bar{\alpha}_{N+1}) \cdot \left(\frac{\Delta N}{2}\right) - \bar{\alpha}_{N+\Delta N} \cdot \left(1 + \frac{\Delta N}{2}\right) = 0 , \tag{25}$$

and the next estimate of the Newton–Raphson scheme, with iterations of index k , is given by:

$$\bar{\alpha}_{N+\Delta N}^{k+1} = \bar{\alpha}_{N+\Delta N}^k - \left(\frac{\partial R_{cj}}{\partial \bar{\alpha}}\Big|_{N+\Delta N}\right)^{-1} \cdot R_{cj} . \tag{26}$$

The residual operator from the Newton–Raphson scheme, a tangent operator used in the iterative search, is expressed as follows:

$$\frac{\partial R_{cj}}{\partial \bar{\alpha}} \Big|_{N+\Delta N} = \frac{\partial \bar{\alpha}_{N+\Delta N+1}}{\partial \bar{\alpha}_{N+\Delta N}} \cdot \left(\frac{\Delta N}{2} \right) - \left(1 + \frac{\Delta N}{2} \right). \tag{27}$$

As in Ref. [25], the only remaining unknown term is $\frac{\partial \bar{\alpha}_{N+\Delta N+1}}{\partial \bar{\alpha}_{N+\Delta N}}$, indicating the variation of the extrapolated quantity at the end of a cycle with respect to the variation of the Newton–Raphson estimate of the quantity at the beginning of the cycle. Using Eq. (8b), we can express the cumulated mechanical energy α_{N+1} at the end of a cycle as:

$$\bar{\alpha}_{N+1} = \bar{\alpha}_N + \int_N^{N+1} \langle \dot{\alpha} \rangle^+ dt. \tag{28}$$

The influence of $\bar{\alpha}_N$ on the evolution of α during a cycle is neglected, as it is small compared to its cumulated value, thus yielding a very simple expression for the tangent operator (27) $\frac{\partial \bar{\alpha}_{N+\Delta N+1}}{\partial \bar{\alpha}_{N+\Delta N}} = 1$.

The full algorithm for this iterative cycle jump scheme is presented in Algorithm 2. In the first step, there is only information on the control cycle N . We start with a simple extrapolation scheme to obtain a first estimate at $N + \Delta N$:

$$\bar{\alpha}_{N+\Delta N} = \bar{\alpha}_N + \Delta N \dot{\bar{\alpha}}_N. \tag{29}$$

From this estimate, a control cycle at $N + \Delta N$ is computed giving an initial residue and starting the presented Newton–Raphson iterative scheme. The iterative scheme is stopped when the maximum value of R^{cj} on the whole domain reaches a specific threshold. The user can then decide at which precision the trapezoidal extrapolation scheme is to be enforced. We chose this precision criterion to be normalized by the initial value of $\bar{\alpha}_N^0$. The convergence criterion can be written as:

$$\max[R_{cj}^{CONV}] < \max[\bar{\alpha}_N^0] \cdot 10^{-6}. \tag{30}$$

Algorithm 2 Cycle jump scheme

Require: $\bar{\alpha}_{N+1}, \bar{\alpha}_N$ with (1)

- 1: Explicit prediction with Eq. (29) to estimate $\bar{\alpha}_{N+\Delta N}^0$
- 2: Compute one cycle to obtain $\bar{\alpha}_{N+\Delta N+1}^0$
- 3: Deduce residual R_{cj}^0 with Eq. (25)
- 4: $\bar{\alpha}_{N+\Delta N}^k \leftarrow \bar{\alpha}_{N+\Delta N}^0$ and $R_{cj}^k \leftarrow R_{cj}^0$
- 5:
- 6: **while** Criterion (30) is not respected **do**
- 7: Find a new estimate $\bar{\alpha}_{N+\Delta N}^{k+1}$ with Eq. (26)
- 8: Compute one cycle to obtain $\bar{\alpha}_{N+\Delta N+1}^{k+1}$
- 9: Deduce residual R_{cj}^{k+1} with Eq. (25)
- 10: **end while**
- 11:
- 12: Next computations initialized with
 $\bar{\alpha}_{N+1} \leftarrow \bar{\alpha}_{N+\Delta N+1}$ and $\bar{\alpha}_N \leftarrow \bar{\alpha}_{N+\Delta N}$

It is interesting to note that for most simulated cases the initial step of fatigue crack propagation can be skipped with a very large ΔN . Indeed, until the fatigue degradation function $f(\bar{\alpha})$ becomes activated, *i.e.*, while $\bar{\alpha} < \alpha_r$, the evolution of $\bar{\alpha}$ is linear. This is used in Ref. [17] to accelerate the initial phase of the simulation.

Moreover, in Kristensen et al. [41], an explicit cycle jump scheme, relying on a backward-Euler extrapolation scheme, is used to accelerate significantly phase-field fatigue computations. The comparison of these schemes is out of the scope of this work (and is detailed in Ref. [25]), but it could be interesting to see if this extrapolation scheme is able to recover accurate results in the proposed adaptive mesh refinement context. This explicit extrapolation scheme trades accuracy for efficiency, and hence requires to use very small values of ΔN in order to minimize error [41]. It is not clear which scheme is more efficient in a coupling context, at a given level of accuracy.

5. Mesh refinement strategy

Adaptive mesh refinement strategies are frequent in crack propagation modeling with a finite element framework because of the very local nature of the damage mechanics. Only a limited part of the structure under study exhibits nonlinear behavior, with high gradient zones localized in that area. To capture the mechanisms driving crack propagation, different levels of mesh refinement are used: coarser elements far away from the damaged zone and finer elements in the vicinity of the crack. This leads to a significant increase in computational efficiency by allowing us to optimize the number of degrees of freedom while maintaining the accuracy of the numerical solution. Furthermore, since the path of the cracks is often unknown in advance, the ability to adapt the mesh

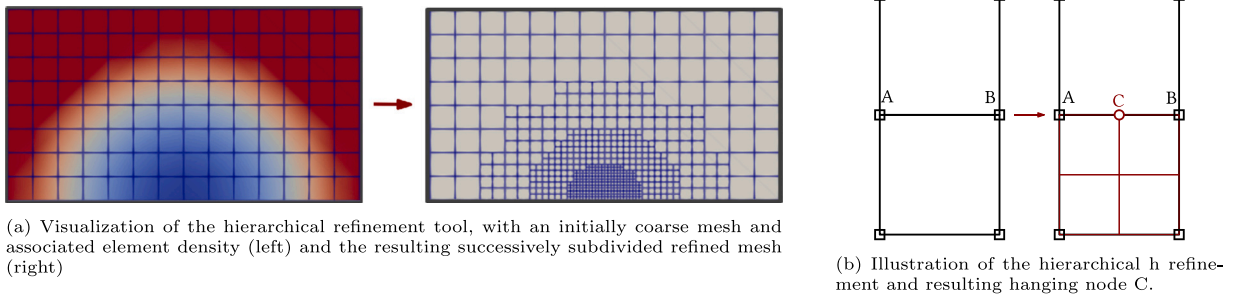


Fig. 4. Figures illustrating non-conforming hierarchical h refinement.

during crack propagation is a valuable technique for further reducing computational effort. For instance, we can cite multiple references that use mesh optimization methods to model crack propagation, such as a combination of XFEM and a localized multi-grid approach [42,43], or XFEM and adaptive mesh refinement [36].

In phase-field modeling different refinement levels should also be used, as d varies between 0 and 1 very abruptly in a local zone whose size is driven by l_c . Multiple analyses of the numerical errors related to space discretization of the phase-field model can be found in the literature [26,44,45]. A fine mesh size in this zone is required to capture the gradient of d in the damage problem, as was analyzed in Ref. [44] where the author showed that $l_c/2 > h$ in the damage zone suffices to recover analytical results. However when damage interacts with the mechanical problem, it does so through the integration points of the finite element mesh, creating a new source of mesh dependent error, known as localization error, that is well understood in the literature [26]. The localization error can be minimized by enforcing larger l_c/h ratios, as far as 8. In this context, adaptive mesh refinement tools have been implemented to make the method practical for industrial applications, where using a high level of refinement across the entire numerical sample would result in an excessive computation time.

For this reason, mesh refinement tools have been developed early for phase-field simulations, as the diffuse representation of cracks requires a very fine mesh to accurately capture the steep gradient of damage in this area. We cite the work of Heister et al. [46], who used adaptive mesh refinement (AMR) on a phase-field model for brittle fracture. Following this, similar damage-driven methods have been proposed [47–49], where multiple damage thresholds were defined to smooth out the mesh transition. More recently, several energy-based criteria specific to phase-field simulations have been highlighted [50,51]. Furthermore, sophisticated phase-field error estimators, in line with usual AMR estimators, have been studied [52,53]. However to the best of our knowledge, AMR framework has yet to be applied in a fatigue fracture phase-field context.

The following section describes the mesh refinement tools that have been implemented to combine the cycle jump scheme with adaptive mesh refinement in the context of phase-field fatigue simulations. The refinement method and projection operator are introduced, followed by the specification of the refinement criterion that was used during the mesh adaptivity process. Finally, we put forward a propagation algorithm rendering it possible to use AMR, and cycle jump simultaneously in the phase-field framework.

5.1. Mesh refinement method

Following Ref. [36], we used hierarchical h refinement: to obtain a given mesh size, coarser elements were subdivided into 2^D finer elements. In 2D, one square element was divided into $2^2 = 4$ elements, in 3D, it was divided into $2^3 = 8$ elements. An illustration of this type of refinement is provided in Fig. 4(a). Furthermore, it should be noted that this hierarchical refinement is non-conforming, meaning that every new subdivided element adds a number of so-called “hanging-nodes”, *i.e.*, nodes that do not respect the continuity of the finite element mesh. They are illustrated in Fig. 4(b). To enforce the compatibility of these nodes with the rest of the mesh we set displacement and damage to be linear combinations of the neighboring nodes displacement and damage using Lagrange multipliers. More details on the used operations can be found in Refs. [36,54]. The hierarchical, non-conforming refinement approach presents numerous benefits within the context of an adaptive mesh refinement framework. Firstly, it makes it possible to keep a memory of original coarse elements, and its different subdivided parts, enabling easy implementation and data structure. Moreover, this refinement technique simplifies the transfer of fields when restricted to mesh refinement, as each finer element is fully contained within a coarser one. Indeed, as field transfers are supported by the finite element shape functions, we find that the hierarchical refinement method enables a trivial link between the shape functions of coarse and fine elements.

In addition, the re-meshing process is designed to enforce a smooth transition between coarse and refined zones. In a hierarchical refinement setting, a coarse element might be divided into n smaller elements while its neighboring element remains coarse. This would introduce strong mesh distortion and yield less precise results. To ensure a smooth progression of subdivisions in neighboring elements, we enforced a “2-to-1” constraint: if a fine element was divided into $n \cdot 2^D$ smaller elements, then its neighboring elements would be divided into $(n \pm 1) \cdot 2^D$. This results in only one “hanging node” (a node on a finer element that is not connected to a node on a coarser element) at each refinement transition. Note that this smoothing process yielded asymmetric patterns of refined mesh even in the case of a seemingly symmetric damage field (Fig. 5). Indeed, it was based on the selection of elements bordering the located damaged zone. Such an automatic selection means that any small asymmetry of the damage field or initial mesh was magnified by the smoothing process. Nevertheless, as will be shown in Section 6, this versatile implementation means that it can recover complex crack patterns without needing to locate the crack tip.

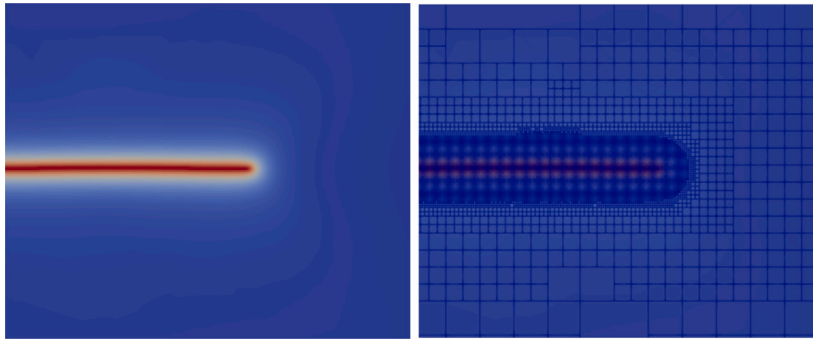


Fig. 5. Illustration of the used refinement strategy on a given damage field.

5.2. Projection process

As the crack propagates, new successive meshes are built to optimize the number of degrees of freedom in real time. This means that for every new refinement step, all quantities defined in the phase-field fatigue framework have to be transferred or re-computed on each new successive mesh pattern. We chose to transfer the following fields: $\bar{\alpha}$, H , and d . The latter was a nodal field that could be trivially interpolated on the newly refined mesh nodes, while $\bar{\alpha}$ and H were defined on integration points and needed a specific projection operator. In the elastic small displacement context we followed the work in Ref. [55], where shape functions of the coarse elements were used to interpolate integration points quantities. Thus, we first transformed those fields into nodal equivalents, and used the coarse element shape function to interpolate the nodal components. Algorithm 3 illustrates this procedure which is a built-in function of Cast3M. The implementation was facilitated by the fact that refined elements are always contained within a larger coarse one.

Algorithm 3 Projection of integration point quantities a

- 1: Coarse mesh M^l is refined into M^{l+1}
 - 2: Every new integration point of coordinate \mathbf{x}^{l+1} is contained into a coarse element E^l , of shape function vector \mathbf{N}_l
 - 3: Nodal vector $\hat{\mathbf{a}}^l$ is constructed by solving $\int_{E^j} \mathbf{N}_l^T \mathbf{N}_j \hat{\mathbf{a}}^l dV = \int_{E^j} \mathbf{N}_l^T \mathbf{a}^j dV$
 - 4: \mathbf{a}^{l+1} is interpolated at \mathbf{x}^{l+1} using $\hat{\mathbf{a}}^l$ and \mathbf{N}_l : $\mathbf{a}^{l+1}(\mathbf{x}^{l+1}) = \mathbf{N}_l(\mathbf{x}^{l+1})\hat{\mathbf{a}}^l$
-

The remaining fields were computed back from the interpolated quantities. In the context of refinement, this projection operator resulted in highly accurate outcomes. However, if this approach were to be applied to coarsening operations, a more sophisticated projection strategy would need to be developed. Coarsening meshes goes beyond the scope of this work, as in phase-field formulation, a fine discretization of the damaged zone has to be enforced for the entire duration of the simulation.

After this projection step, $\bar{\alpha}$, H , and d did not unify the balance equation. This may lead to numerical errors that can be amplified ΔN times if a cycle jump procedure is applied to the resulting imbalanced fields. To prevent this, we computed an equilibrium step after each projection step, consisting in the computation of a cycle without cumulating α , hence enforcing mechanical/damage equilibrium without propagating the damage further. It should be noted, that such a balancing step is common when using the presented projection strategy, as is underlined in Refs. [36,56].

As irreversibility is enforced through the history-field method introduced in Section 2.5, H is continuously compared to computed mechanical energy to set irreversibility. However, such a local irreversibility check is impossible from one mesh to another as we cannot compare values on nodes/integration points that did not previously exist. As such, every time a new mesh is built, and the fields projected, we checked that $W(d)$ did not decrease. This verification was done on the global quantity $W(d)$ as we were unable to get local corrections on the history field. In practice, no reversibility of the damage field was observed in Section 6.

5.3. Refinement criterion

Finally, it is necessary to establish a refinement criterion that, given a particular crack topology, will allow for the determination of a target mesh density that balances the number of degrees of freedom with an appropriate level of precision. In a finite element framework, one traditionally uses estimators relying on gradient quantities. However, we employed a simpler approach, considering damage as the critical field to describe. As a result, it was imperative that the zone affected by damage was refined to a very high degree. As stated, high l_c/h ratios had to be reached in the zone where damage localizes in order to minimize the numerical error. Consequently, we set the following refinement criterion: if $d \geq d_{AMR}$, then $h = h_{AMR}$, with the parameters:

1. d_{AMR} : a threshold of damage that defines the boundary of the damaged zone,
2. h_{AMR} : a mesh size prescribed in this damaged zone.

It should be noted that elements for which d is under the threshold d_{AMR} may also be refined due to the “2-to-1” topological refinement transition.

At cycle N every element of the finite element mesh where at least one nodal value of d exceeds d_{AMR} , has to be of size h_{AMR} . Section 6 presents several values of d_{AMR} and h_{AMR} having been tested in this context. For a given crack, this mesh refinement criterion is illustrated in Fig. 5. Here, we set $d_{\text{AMR}} = 0.1$ and $h_{\text{AMR}} = l_c/8$. A smooth transition between the coarse area and the refined damage zone was achieved by refining successive layers of elements along the damaged zone.

5.4. Algorithm for fatigue crack propagation

To ensure the accuracy of the solution, it is crucial to evaluate the refinement criterion described in Section 5.3 at every computed step across the entire domain. As the crack path is not known *a-priori*, we used an *a-posteriori* verification of the criterion at the end of every computed cycle. If the criterion was not respected, it meant that during the cycle, the convergence of the coupled problem was achieved on a mesh that was not fine enough to capture the damage field precisely. Consequently, the mesh was further refined in the relevant zones, projection and balancing steps were carried out to recompute the cycle on this new mesh. This process was repeated until the criterion was respected at the end of the cycle. Since fatigue crack propagation occurs at a very slow rate over the course of a cycle, it is expected that a limited number of iterations will be necessary to attain a converging mesh. In fact, with a cycle-by-cycle handling of the lifetime prediction, an *a-priori* estimation can be considered. However, in this work we showcase a coupling between adaptive mesh refinement and cycle jump schemes, introducing possible long jumps between two computed cycles. In such cases, the damage zone can propagate further than the refined zone during the cycle jump procedure, rendering an *a-posteriori* criterion check mandatory. This method of combining adaptive mesh refinement with a phase-field model is similar to the approaches outlined in Refs. [46,47,49], as it involves using a damage criterion to drive *a-posteriori* mesh refinement. However, as the method is used along cycle jumps, we propose an AMR criterion check after each jump.

It should be noted that for some numerical cases in Section 6, a cycle-by-cycle approach was used. This meant that step (4) of Algorithm 4 was not performed. In this case, we verified the validity of the AMR criterion after each computed cycles. The implementation of this algorithm will be tested successively on both fixed pre-refined meshes and on coarse meshes that have been refined using AMR during propagation. This will allow for an individual investigation of the mesh refinement and cycle jump schemes.

Algorithm 4 Cycle jump crack propagation with AMR

```

1: for N = 1, Nmax do
2:   while Refinement criterion is not respected do
3:     Computation at cycle N: Alg. 1
4:     Cycle jump scheme to N + ΔN: Alg. 2
5:     Check refinement criterion at N + ΔN
6:     if Remeshing is needed then
7:       Remeshing operations
8:       Projection of the fields at N: Alg. 3
9:       Balancing step at N
10:      Restart step (3) at N
11:     else
12:       Go to next computation step N + ΔN quit
13:     end if
14:   end while
15: end for

```

6. Numerical examples

This section incrementally introduces the adaptive mesh refinement and cycle jump techniques through the examination of well-known benchmark cases. Several 2D geometries are presented to investigate the proposed coupling in terms of precision and efficiency. Additionally, different crack propagation mechanisms are reproduced to showcase the method’s flexibility.

Unless otherwise specified, the presented numerical models do not use the spectral split introduced in Eq. (6), and employ the asymptotic degradation function (9) and 2D plane strain conditions. Two measures of crack length were considered. One was calculated by searching for the maximum extent of the damaged zone with $d \geq 0.95$, and the second, with a measure of crack area, defined in Eq. (4). The former approach was used when only one crack propagates in mode I, *i.e.*, the first 3 samples.

In a majority of the numerical examples presented, a crack was initialized with a “double-node” configuration, signifying that a finite element mesh includes a discrete geometric representation of the crack. Conversely, on the coalescing crack examples, initial cracks were set by enforcing a Dirichlet condition $\hat{d} = 1$ on the relevant nodes. The examination of how the choice of the crack initialization method impacts the structural response is not within the scope of this work. However, for those who are interested, Ref. [57] explores and compares multiple damage initialization methods, while Ref. [30] investigates the effect of different phase-field formulations and initialization approaches.

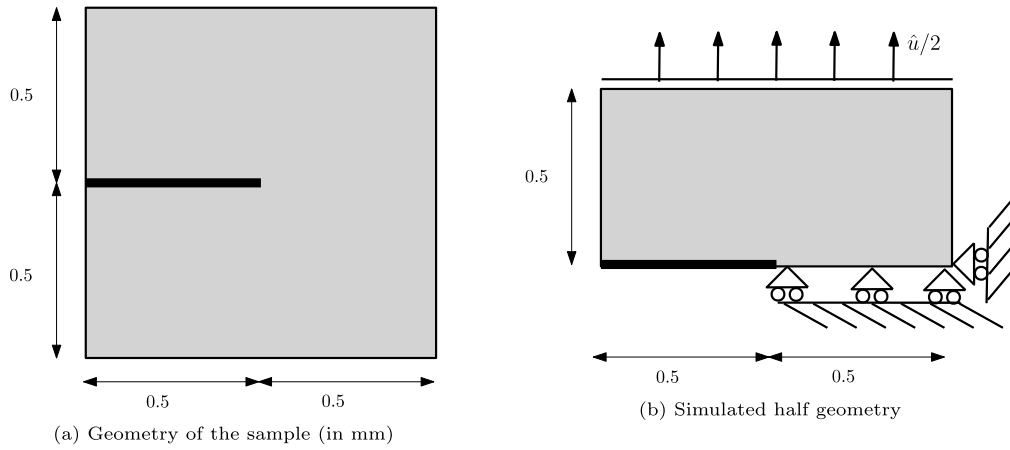


Fig. 6. Geometry, boundary conditions used for the single edge notched tensile test.

Table 1
Absolute computing time on SEN.

AMR	Computing time	Degrees of freedom
Yes	11 h 25	From 2000 to 20000
No	38 h 20	20000

6.1. Single edge notched tensile test

In order to validate the proposed phase-field fatigue implementation, we compared results on the single edge notched tensile test [14,37]. Geometry, boundary conditions and initial crack position are shown in Fig. 6(a). The following material properties were used: $E = 210$ GPa, $\nu = 0.3$, $l_c = 4 \cdot 10^{-3}$ mm, $G_c = 2.7$ N/mm, $\alpha_T = \frac{G_c}{12 \cdot l_c} = 5.625 \cdot 10^7$ N/m². To study fatigue crack propagation, we employed a cyclic loading: a periodic displacement of amplitude $\hat{u}_{max} = 2 \cdot 10^{-3}$ mm and load ratio of -1 . It should be noted that the load ratio is defined as the ratio of minimum and maximum loads in one cycle: $\hat{u}_{min}/\hat{u}_{max}$.

Cycle jump was not used. We compared the results on a fixed mesh refined on the expected crack path prior to the simulation against a mesh updated during crack propagation using the adaptive mesh refinement tool. The AMR tools were set up with $d_{AMR} = 0.1$ and $h_{AMR} = l_c/8$. The two cases are compared in Fig. 7d, e.

The comparison of the evolution of the crack length with the literature is shown in Fig. 8. Our implementation was in good agreement with previous results [14,37]. Additionally, using the proposed mesh refinement tool, the computing time was divided by more than 3 as compared to the case with an *a-priori* refined mesh. Some insights into the absolute computing time of the implemented framework on Cast3M is provided in Table 1. Those computations were executed on 4 cores of a machine with an AMD EPYC 7281, 2.1 GHz CPU.

We studied the influence of both AMR criteria on the relative error in the crack area between AMR and initially refined meshes (PR). This relative error is defined as:

$$Error_{A(d)} = \frac{|A_{PR}(d) - A_{AMR}(d)|}{A_{PR}(d)} \tag{31}$$

Fig. 9 illustrates the error convergence rate with respect to d_{AMR} and h_{AMR} criteria. The plotted data in Fig. 9b suggests that the h_{AMR} criterion significantly impacted the accuracy of computed results. However, Fig. 9a shows that the precision was less affected by the d_{AMR} criterion as opposed to the h_{AMR} criterion. These results were expected [7,8], as a very fine mesh size relative to the length scale was required in order to reach a decent precision. On the other hand, strong refinement further away from the damaged zone was less relevant in order to precisely compute the crack propagation, as illustrated by the low influence of d_{AMR} for $d_{AMR} < 0.5$.

6.2. Mode I crack opening in an infinite plane

Another usual benchmark of fracture mechanics was then studied: mode I opening of a crack in a quasi-infinite plane. The geometry and boundary conditions for this next sample are illustrated in Fig. 10. Only a quarter of the sample was modeled because of symmetry with a refinement of $h = l_c/8$ in the expected damage zone. We used the following material properties: $E = 210$ GPa, $\nu = 0.3$, $l_c = 0.1$ mm, $G_c = 2.7$ N/mm, $\alpha_T = \frac{G_c}{12 \cdot l_c}$.

The first part of the study focused on the precision and efficiency of the cycle jump scheme by itself, which is why adaptive mesh refinement was not used in this example. The fixed mesh was refined prior to the simulation on the expected crack path.

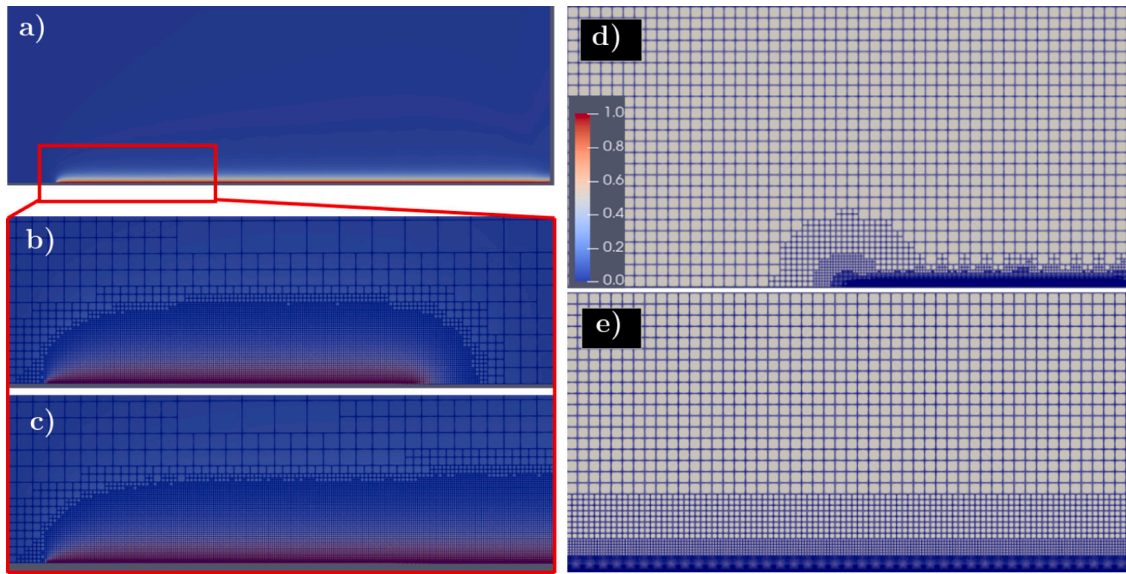


Fig. 7. Visualization of the adaptive mesh refinement tools on the single edge notched specimen. a, b, c, d illustrate the adaptively refined solution. (a) Damage field on the half-specimen (b) Damage field and adaptive mesh in the red zone at cycle N = 50 (c) Damage field and adaptive mesh in the red zone at cycle N = 100 (d) Adaptively refined mesh at N=200 (e) Fixed mesh refined prior to the simulation.

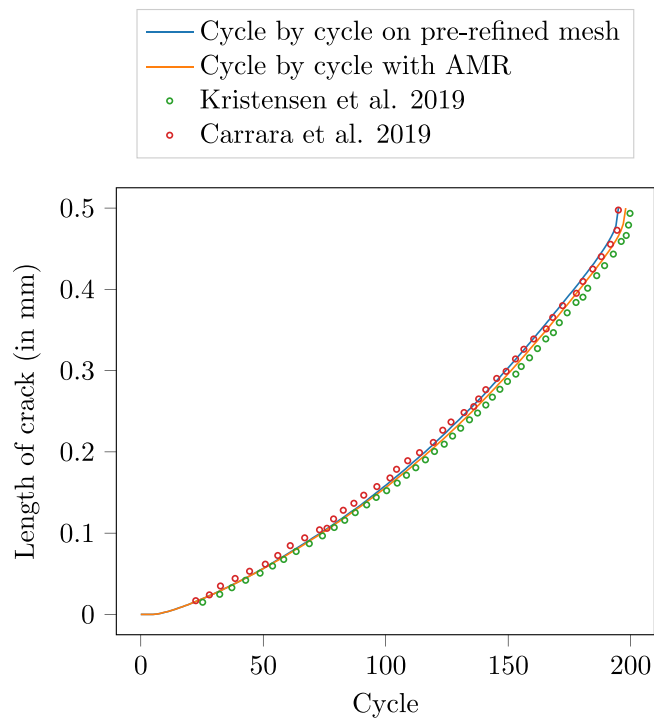


Fig. 8. Length of the crack — comparison with fatigue phase-field literature.

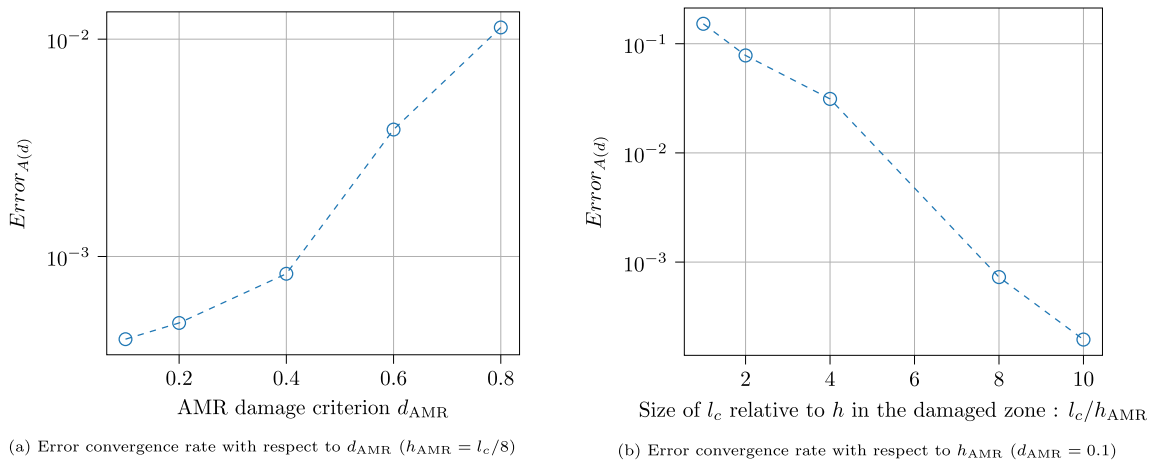


Fig. 9. Error convergence rate with respect to the mesh refinement criteria.

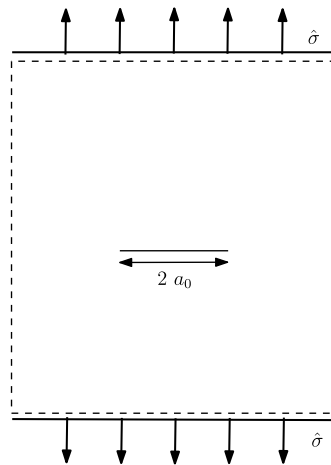


Fig. 10. Geometry of the sample.

Table 2
Efficiency improvements compared to cycle-by-cycle calculation, on a fixed mesh.

Loading case	ΔN	Acceleration factor (T^0/T^{cj})
$\Delta\sigma_2$	30	4.12
$\Delta\sigma_2$	60	4.83
$\Delta\sigma_2$	120	4.56
$\Delta\sigma_2$	240	4.01

A cyclic stress is enforced on its upper boundary with a loading ratio of 0 and a load amplitude of $\Delta\sigma_2 = 40$ MPa. The resulting crack area and cycles per computed time steps with varying ΔN are compiled in Fig. 11. As observed in Ref. [25] the cycle jump scheme was able to recover cycle-by-cycle results independently of the number of extrapolated cycles ΔN . However, it suffered from convergence issues if a large ΔN was used. Indeed, for larger numbers of jumped cycles, many more implicit iterations are required. At ΔN values of 240 and 120, which correspond to approximately 20% and 10% of the total lifetime respectively, non-convergence issues were observed at 700 cycles and 1700 cycles, indicating an acceleration in the rate of fatigue crack propagation. This finding highlights the potential benefits of setting an adaptive value for ΔN using a criterion such as the one described in Ref. [25]. In the event that non-convergence was seen in the cycle jump iteration scheme, we reset the computed time step by using a smaller ΔN value. The gains in computing time are compiled in Table 2. The acceleration factor is here defined as unaccelerated computing time T^0 over cycle jump accelerated computing time T^{cj} .

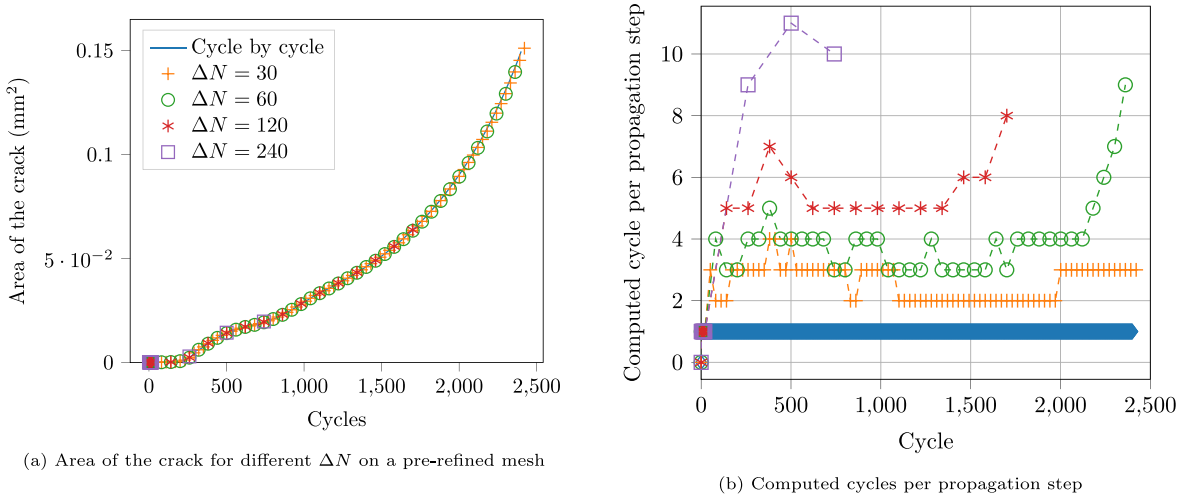


Fig. 11. Study of the influence of ΔN on a pre-refined mesh.

Table 3

Computing gains with cycle jump and AMR tools compared to cycle by cycle on a pre-refined mesh.

Loading case	ΔN	Acceleration factor (T^0/T^{cj+R})
$\Delta\sigma_2$	Cycle by cycle	2.34
$\Delta\sigma_2$	30	7.79
$\Delta\sigma_2$	60	11.69
$\Delta\sigma_2$	120	8.44
$\Delta\sigma_2$	240	6.98

The same process was carried out with adaptive mesh refinement. Hereafter, $d_{AMR} = 0.1$ and $h_{AMR} = l_c/8$ were used as the criteria of refinement. First, results with AMR are compared to results without AMR, hence, the same loading was initially applied. Multiple values of ΔN were tested and precise results were again recovered almost independently of ΔN : the crack area and computed cycles per propagation step are plotted in Fig. 12. However, similar issues of slow convergence of the cycle jump scheme were observed. Furthermore, convergence was even slower and a computing gain threshold was seen for lower values of ΔN . Indeed, with cycle jump, i mesh refinement iterations signified that the cycle jump scheme was restarted i times which could induce a large number of computed cycles per propagation step as is illustrated in Fig. 12b. In this context, an adaptive value of ΔN seemed even more relevant to avoid such issues. Additionally, in the case of multiple mesh refinement iterations, $\bar{\alpha}_{N+\Delta N}$ can be projected and stored to be used as a first estimate of the iterative scheme instead of the explicit extrapolation (29). Such operations slightly reduced the number of iterations of the cycle jump scheme for each further mesh refinement step. As before, gains in computing time were compiled in Table 3, where the acceleration factor was defined as unaccelerated computing time T^0 over cycle jump and AMR accelerated computing time T^{cj+R} .

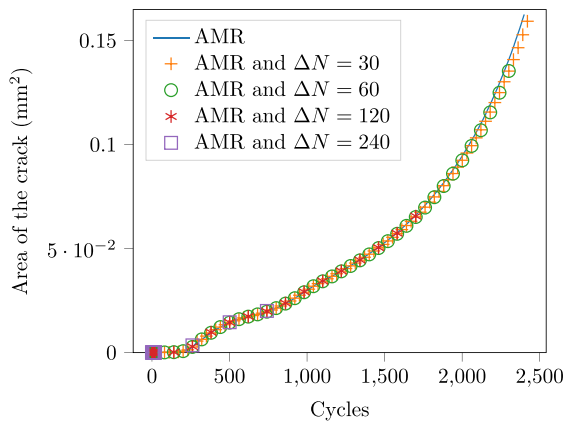
Successive images of the damage field and mesh during propagation with AMR and cycle jumps, are provided in Fig. 13. Every image corresponds to one propagation step.

Finally, we wished to investigate the scalability of the method in the case of larger fatigue lifetimes. Hence, three other applied loadings were tested, $\Delta\sigma_1 = 60$ MPa $\Delta\sigma_3 = 20$ MPa, $\Delta\sigma_4 = 10$ MPa. Gains in computing time for these three cases are compiled in Table 4. The acceleration factor was here defined as the AMR cycle-by-cycle computing time T^{AMR} over AMR and cycle jump accelerated computing time T^{cj+R} .

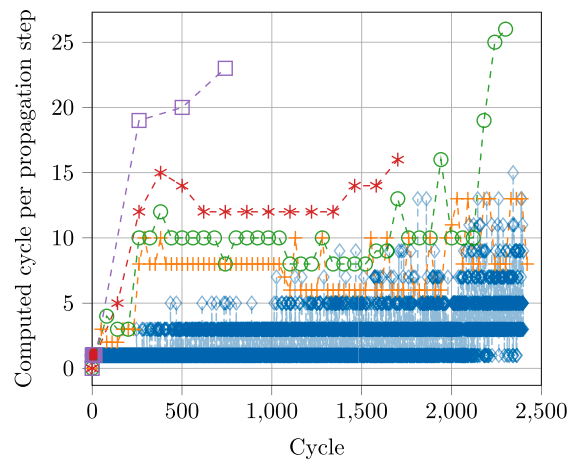
The performed computations induced four different crack propagation speeds, illustrated in Fig. 14a. As demonstrated by Carrara et al. [14], the fatigue model used in this study exhibited characteristics consistent with the Paris law theory. This implies that a linear regime dependent on material properties can be identified when plotting the crack propagation speed (da/dN) against the variation in stress intensity factor (ΔK). Indeed, for the four loading scenarios resulting in the crack growth plotted in Fig. 14a, we followed the guidelines of ASTM recalled in Carrara et al. [14], to identify the related crack growth rate curves. We observed a load-independent linear regime, as can be seen in Fig. 14b., that we related to a Paris regime.

6.3. Compact tension sample

In this section we follow the process of Gibert [58], where a compact tension (CT) geometry is studied numerically and experimentally. Subsequently, to examine the impact of mixed mode crack propagation, a hole was punched in a CT geometry



(a) Area of the crack computed for different ΔN on an adaptively refined mesh



(b) Cycles computed per propagation step

Fig. 12. Study of the influence of ΔN on an adaptively refined mesh.

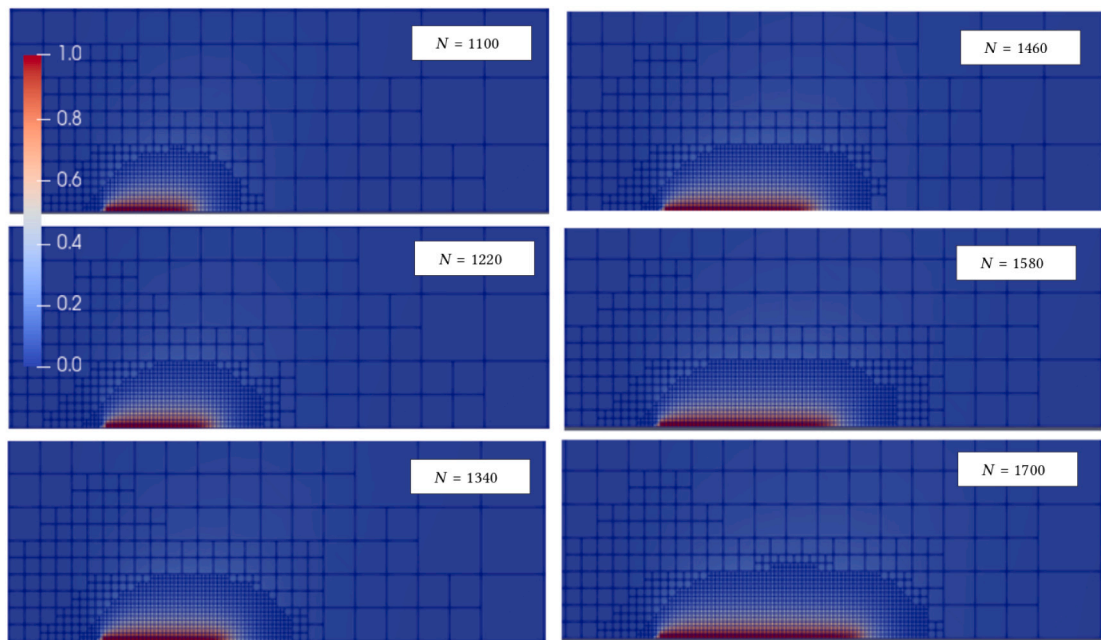
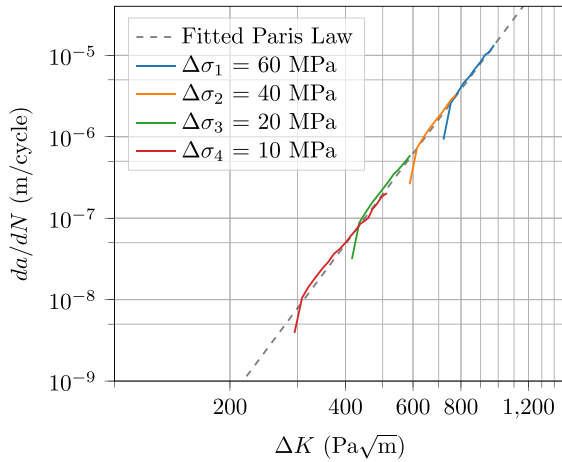


Fig. 13. Visualization of the adaptive mesh refinement coupled with cycle jump tools on the crack in an infinite plane.

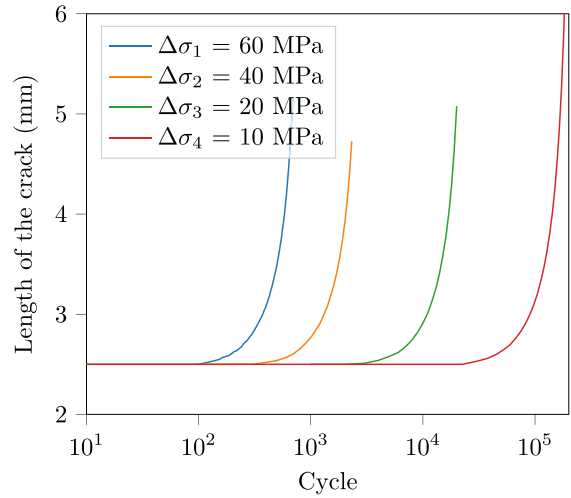
similar to the one used in the previous analysis. Accordingly, in our work, the CT geometry was used to calibrate the model. Then, the perforated geometry was employed to evaluate the predictive ability of the model with this calibration.

As shown for the previous numerical sample, a Paris regime can be associated to numerical parameters. Hence it is possible to fit those parameters to specific material coefficients for Paris' law and reproduce experimental data. Such a fit, in the context of numerical-experimental comparison, was done in the following Refs. [19,21,25]. As a matter of fact, in this last reference, the authors underlined the high computational cost associated with the calibration of Paris' law, justifying the need for accelerating methods such as cycle jump schemes.

Consequently, in this section we fit numerical parameters of the phase-field fatigue model to material coefficients obtained experimentally in Ref. [58] on a CT sample. Using these fitted parameters, the perforated CT sample was then simulated under similar loading conditions. Finally, the computed and experimental crack paths were compared.



(a) Crack length as a function of computed cycle for different loading



(b) Same result in the Paris domain

Fig. 14. Observation of a linear regime independent of applied load.

Table 4

Computing gains with cycle jump and AMR tools, compared to cycle-by-cycle/AMR.

Loading case	ΔN	Acceleration factor ($T^{\text{AMR}}/T^{\text{c}+\text{R}}$)
$\Delta\sigma_1$	10	1.20
$\Delta\sigma_1$	15	1.15
$\Delta\sigma_1$	35	1.12
$\Delta\sigma_1$	70	1.12
$\Delta\sigma_2$	30	2.85
$\Delta\sigma_2$	60	4.99
$\Delta\sigma_2$	120	2.98
$\Delta\sigma_2$	240	3.32
$\Delta\sigma_3$	212	16.73
$\Delta\sigma_3$	525	18.87
$\Delta\sigma_3$	1050	14.61
$\Delta\sigma_3$	2100	14.09
$\Delta\sigma_4$	2500	113.35
$\Delta\sigma_4$	5000	157.52
$\Delta\sigma_4$	10000	136.13
$\Delta\sigma_4$	20000	130.83

To enable flexibility of the numerical fit, we used Carrara’s logarithmic degradation function (10) which gave us two degrees of freedom to influence the fatigue degradation function: α_T and κ . It should be noted that the physical meaning of the brittle phase-field numerical parameters, i.e., G_c and l_c , while actively debated in the literature, remain out of the scope of the present work. Indeed, the numerical fit was carried out by optimizing the values of G_c , l_c , α_T and κ simultaneously.

The CT sample was first modeled to observe the influence of the given parameters on the Paris regime. The geometry of the sample is shown in Fig. 19 (without the hole) and the used mesh is given in Fig. 15. The thickness of the experimental sample was 12.5 mm, and a 2 mm pre-crack was created prior to the experimental study. The material parameters used were: $E = 210$ GPa, $\nu = 0.3$. Using the process illustrated in Fig. 14b, three loading scenarios were computed for the same geometry and the crack growth rate curves were extracted. The material coefficients related to Paris’ law were then deduced by identifying the emerging linear regime. Denoting C and m the Paris law coefficients in Fig. 1, we found similar results to those of Seles et al. [17]: a correlation between α_T and C and a correlation between κ and m . Figs. 16 and 17 show plots of the linear regime computed respectively for varying κ and varying α_T .

The physical interpretation of the numerical parameters was not a factor in the applied fit. The four coupled unknowns, d , G_c , κ and α_T where tuned in order to reach a good correspondence between the fitted model and the experimental results in Ref. [58]. In this process, we used the link between Paris law coefficients and κ , α_T to fine-tune initial results.

Accordingly, we fit our model to the experimental results of Ref. [58], with $l_c = 0.1$ mm, $G_c = 80$ N/mm, $\alpha_T = 10^9$ N/m² and $\kappa = 0.8$. With those fitted parameters, an applied loading of $\hat{F}_{\text{max}} = 20$ kN and a loading ratio of 0.1, we reproduced the experimental results of crack length with respect to the elapsed cycle in Fig. 18.

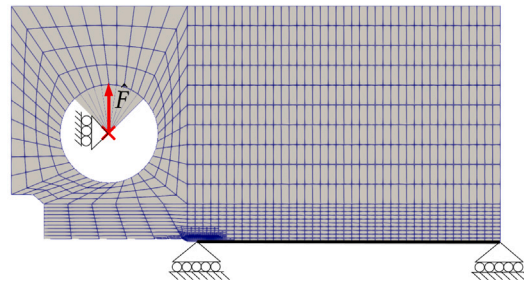


Fig. 15. Initial mesh and boundary conditions.

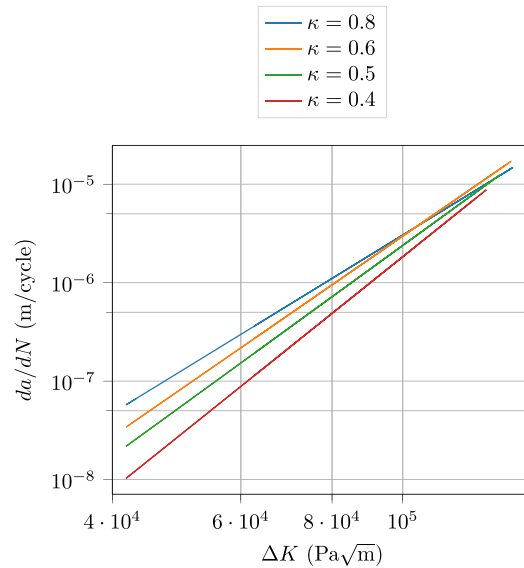


Fig. 16. Influence of κ on identified Paris law.

Finally, the fitted numerical parameters are applied to the perforated CT model. The same loading of $\hat{F}_{max} = 20$ kN, and loading ratio 0.1 were employed. Following Ref. [58], two hole diameters were tested on the CT geometry. The geometry of the sample with the hole is presented in Fig. 19. The position and diameter of the hole used in the analysis are summarized in Table 5. We studied the influence of the hole diameter on the crack path by running two simulations of the perforated CT.

In Geometry 1, the crack deviated slightly from its usual path. In contrast, the crack was completely attracted to the hole in Geometry 2, where a larger hole had been drilled. These experimental observations were reproduced numerically with the previous fit. Fig. 20, illustrates this numerical-experimental comparison. On the left, we see the numerical results of the proposed model superimposed with the experimentally obtained cracks represented as black dashed lines. On the right, we picked figures from Ref. [58]. The experimentally measured displacement field is shown superimposed with the author’s numerical results in white. One can see that a different initial crack height was recovered as the parameters of the hole given in Table 5, were slightly different from the final experimental geometry, due to usage of a low precision machining process [58]. Finally, images of the damage field on the adaptively refined meshes are illustrated in Fig. 21. These numerical observations showed that a given Paris law fit could be transferred to another geometry with this model, and still yield relevant results.

It should be noted that no precise prediction could be made in this study. Firstly, as indicated in Ref. [58], plastic effects played a significant role on the results obtained for this material under the given loading conditions on the CT sample. Additionally, in the current fitting process, the choice of l_c and G_c was arbitrary, although they could typically be linked to fracture mechanics quantities in case of brittle fracture. Ultimately, this study serves as a proof of concept where the experimental results were qualitatively reproduced through the use of AMR and cycle jump acceleration in the numerical fit of the perforated CT.

6.4. Crack branching

We wanted to show that the crack branching phenomenon could be simulated by the present model and guarantee accuracy with the AMR and cycle jump coupling. Therefore, we introduced a case study inspired by Molnár & Gravouil [8], where a notched

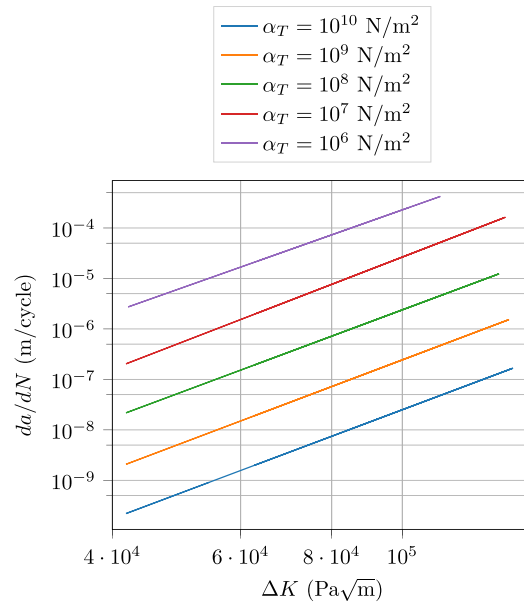


Fig. 17. Influence of α_T on identified Paris law.

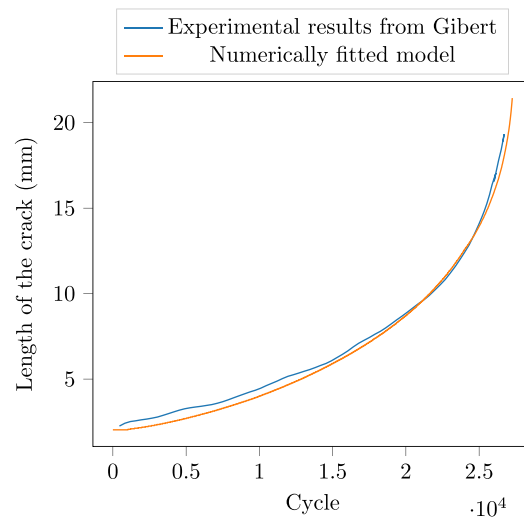


Fig. 18. Length of the crack with the compact tension geometry.

Table 5
Geometric properties of the holes, from Ref. [58].

	x_1	y_1	d_1
Geometry 1	18 mm	7 mm	4 mm
Geometry 2	18 mm	7 mm	5.3 mm

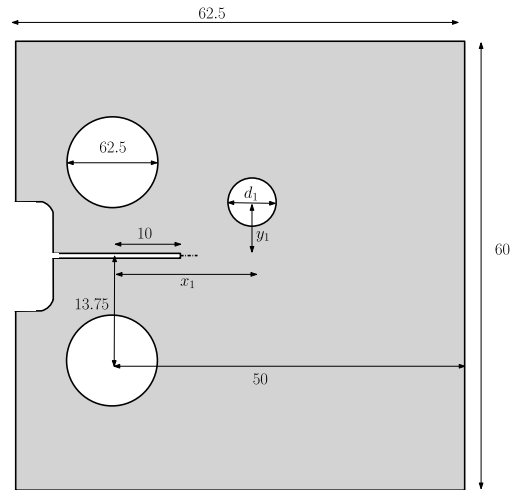


Fig. 19. Compact tension specimen geometry, with a hole (in mm).

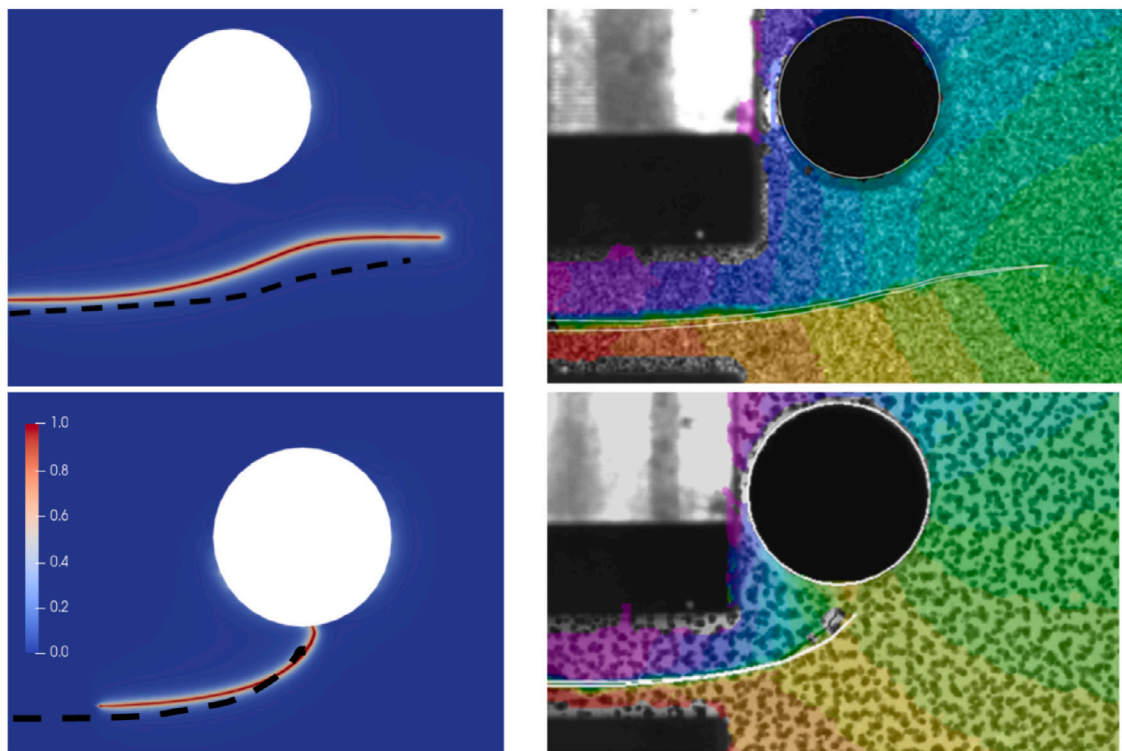


Fig. 20. Comparison of crack paths with the numerical fitted model (left) and experimental-numerical results by Gibert [58] (right). The first row corresponds to geometry 1 and the second row to geometry 2.

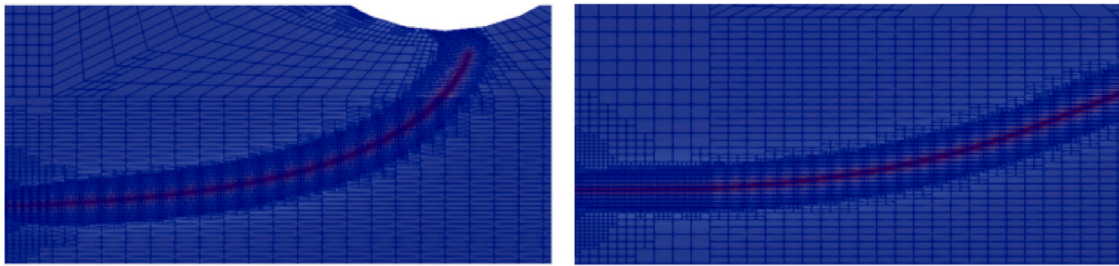


Fig. 21. Meshes obtained with Algorithm 4 on geometry 1 (left column) and geometry 2 (right column).

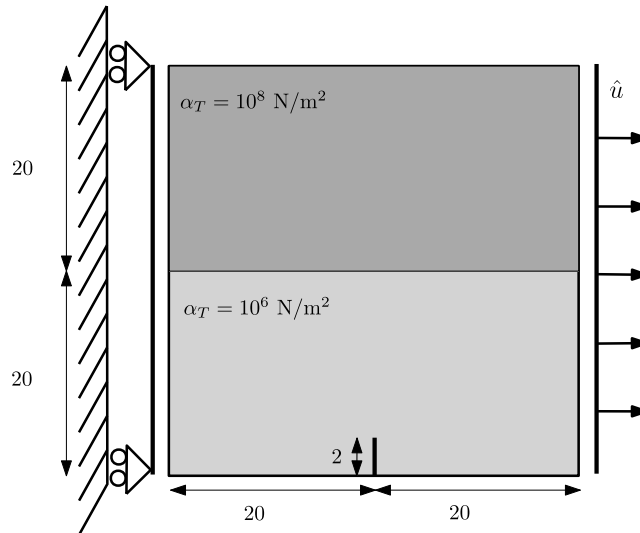


Fig. 22. Geometry (in mm) and boundary conditions.

bi-material sample was used to display crack branching. Here, the bi-material illustrated in Fig. 22 consisted of two fictive materials differentiated by their fatigue threshold α_T . During cyclic loading, we anticipated crack propagation to occur perpendicular to the load direction until the interface between the upper and lower materials was reached. Once this point was attained, crack branching was observed due to the inability of damage to occur in the much tougher upper material.

Other than α_T , both materials had the same properties: $E = 210 \text{ GPa}$, $\nu = 0.3$, $l_c = 0.3 \text{ mm}$, $G_c = 1 \text{ N/mm}$. A cyclic loading of maximum amplitude $4 \cdot 10^{-3} \text{ mm}$ and load ratio 0 was applied.

A pre-refined mesh was utilized for cycle-by-cycle time discretization. It was refined on the expected crack path and the bi-material interface with $h < l_c/2$ in the refined zone. Next, a model is employed with a pre-refined mesh limited to a small zone around the initial crack tip. A similar density of element $h_{AMR} < l_c/2$ was enforced, and $\Delta N = 200$ cycles was initially used.

Fig. 23 compares the crack areas for the two models as a function of elapsed cycles. In this scheme we can observe the multiple crack propagation regimes that the present geometry enabled. Indeed, from cycle 0 to 8500, tensile fatigue crack propagation was observed until the crack reaches a critical length that triggered unstable propagation. As previously demonstrated, the current model could simulate both fatigue crack propagation and unstable brittle fracture [14]. For this particular geometry, we demonstrated that our implementation could also reproduce such cases, even with the aid of AMR and cycle jump tools. It should however be noted that uneven damaged zones were present on the unstable crack pattern in Fig. 24, revealing issues in the present algorithm in the case of unstable crack propagation. Still, these spurious results seemed to have a minimal effect on precision as shown in Fig. 23 where a small deviation was observed at instability.

Finally, when the crack reached the interface of the bi-material, it branched. At this interface, crack propagation slowed down significantly and we could observe the creation of two crack tips propagating in opposite directions. The evolution of the mesh with AMR and cycle jump tools is represented in Fig. 25. These numerical experiments confirmed the ability of the model when it comes to dealing with multiple crack tips and the crack branching phenomenon, without additional treatment. Furthermore, we observed that the accelerated model ran 3.55 faster than the cycle-by-cycle fixed mesh model.

6.5. “En-passant” geometry

This section investigates the precision and gain in efficiency of the method on a complex multi-crack scenario. Inspired by references [8,59,60], the “en-passant” geometry was used to combine mixed mode propagation and crack coalescence. Geometry

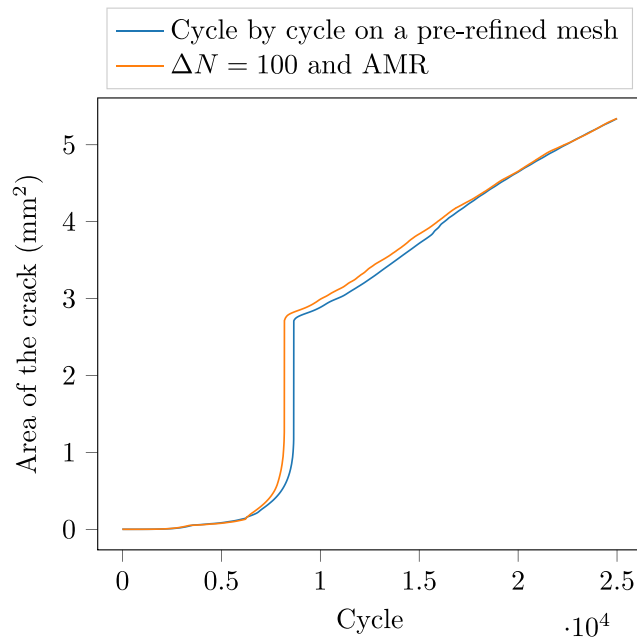


Fig. 23. Area of the crack with and without acceleration tools.

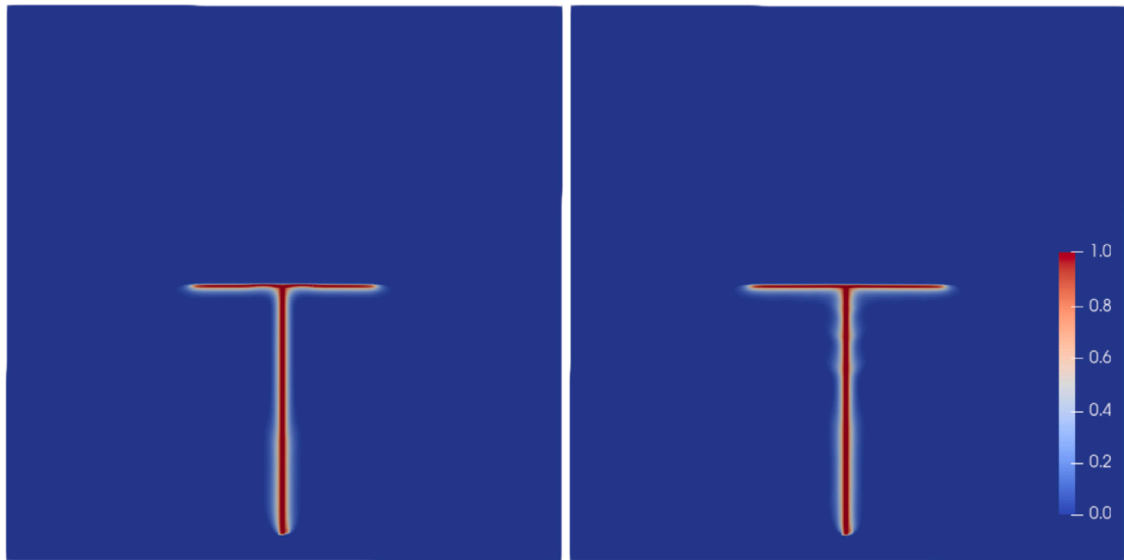


Fig. 24. Damage field after 25000 cycles on base model (left), and accelerated model (right).

and boundary conditions are detailed in Fig. 26a. Contrary to all other numerical samples, the initial crack was not prescribed as double nodes, but as Dirichlet conditions $\hat{d} = 1$ on initially damaged nodes. Material properties were $G_c = 2.7 \text{ N/mm}$, $l_c = 5 \cdot 10^{-3} \text{ mm}$, $\alpha_T = 540 \text{ N/m}^2$, $E = 210 \text{ GPa}$ and $\nu = 0.3$. A cyclic loading was applied to the upper edge of the amplitude $\Delta u = 5 \cdot 10^{-4} \text{ mm}$ and the loading ratio was 0. We compared results obtained on a fixed mesh refined prior to the simulation with $h < l_c/2$ in the refined zone, and $\Delta N = 500$, to results obtained with AMR such that $d_{\text{AMR}} = 0.1$, $h_{\text{AMR}} < l_c/2$ and $\Delta N = 2000$. The initial meshes are illustrated in Fig. 26b.

The computed area of the crack is provided in Fig. 27, and the damage fields on successive meshes are compiled in Fig. 28. The crack area and pattern were very close in both configurations. Moreover, the expected crack interactions are recovered and were found to be similar: the crack tips repelled each other before an attracting phase. These observations were in line with the referenced experimental and numerical simulations [8,60]. It should be noted that the fully accelerated simulation (AMR and cycle jump, with $\Delta N = 2000$) ran more than twenty times faster than the semi-accelerated simulation (No AMR and $\Delta N = 500$).

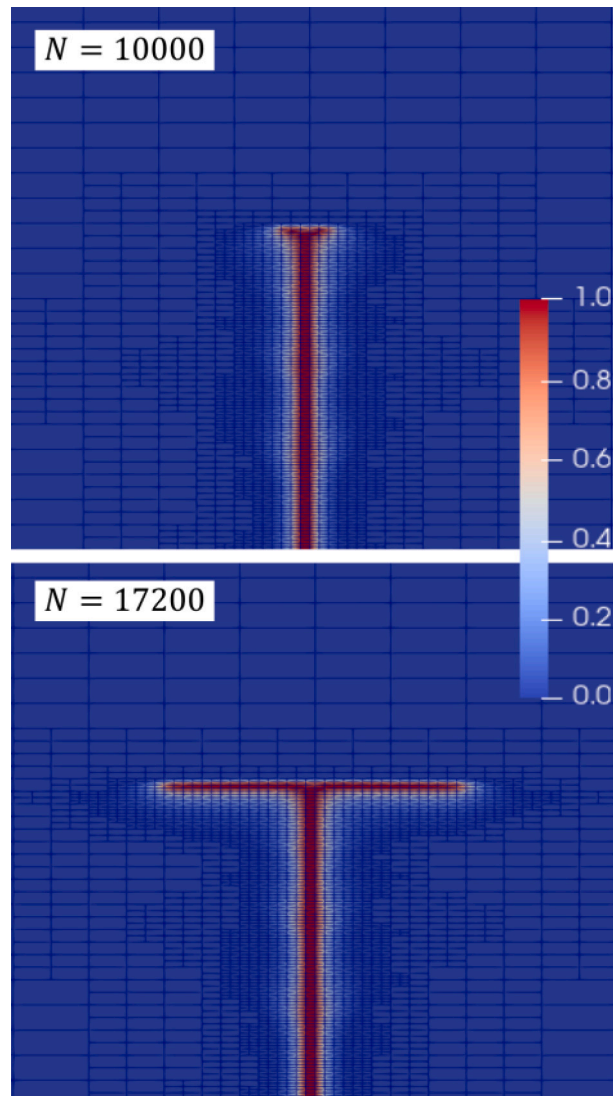


Fig. 25. Damage field on successive meshes for the AMR and cycle jump accelerated model.

6.6. Crack nucleation

On this last numerical sample we wanted to show that the current framework was able to recover cases of crack nucleation with no initial crack tip, notch or damaged zone. Indeed, the ability to model fatigue crack nucleation and growth in a single framework could bridge the gap between usual complete fatigue life analysis and fatigue crack propagation methods. In order to trigger crack nucleation in a homogeneous unbroken structure we mirrored the following Refs. [14,61–63], that investigated crack nucleation on a periodically perforated plate: the geometry and boundary conditions are compiled in Fig. 29. The material properties were $E = 12$ GPa, $\nu = 0.3$, $l_c = 0.01$ mm, $G_c = 1.4$ N/mm, $\alpha_T = 6.48$ N/m². A cyclic displacement was enforced on the upper edge which compressed the structure, $\hat{u}_{\max} = -2 \cdot 10^{-3}$ mm with a load ratio of 0. On this sample the spectral split introduced in Eq. (6) was used.

A mesh pre-refinement equivalent to $h < l_c/3$ was enforced around the holes. During computations, the following criteria were used $h_{\text{AMR}} < l_c/6$, $d_{\text{AMR}} = 0.1$ and $\Delta N = 20$. Fig. 30. shows an image of the damage field after crack initiation. As was observed experimentally, vertical crack patterns emerged in most holes. However, spurious zones of damage were also seen perpendicular to the applied loading and on a cross pattern centered around the hole. These results were in line with Ref. [62] (where a spectral split was also used, on a brittle fracture case, *i.e.*, with a monotonous loading).

By contrast, experimental studies of such a geometry on a quasi brittle material only showed vertical cracks [61]. In fact, these spurious damaged zones were due to the adopted spectral split, which, as observed in the literature, is not always well suited to

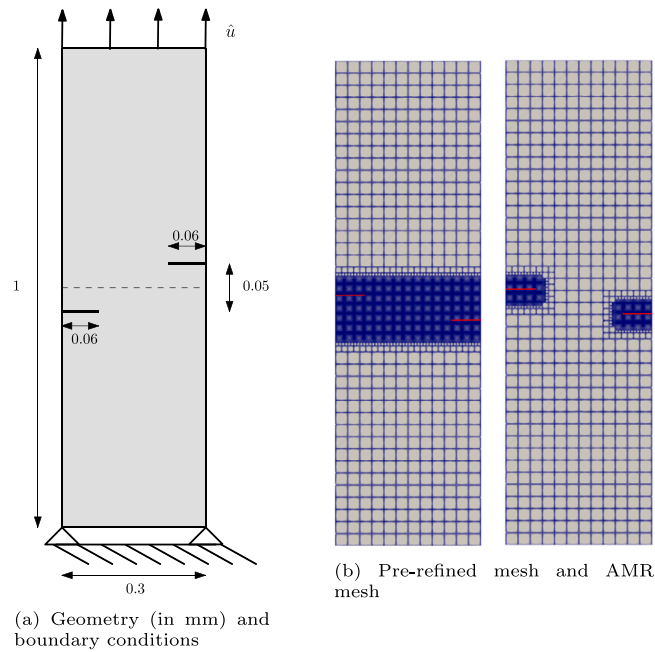


Fig. 26. Fixed mesh and AMR initial mesh used for the “en-passant” sample. Red markers correspond to nodes where $\hat{d} = 1$ is enforced.

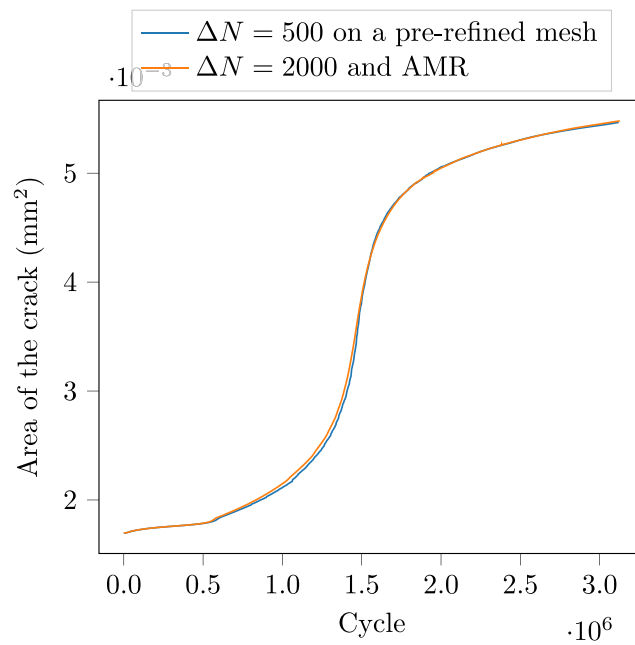


Fig. 27. Area of the crack with respect to elapsed cycle.

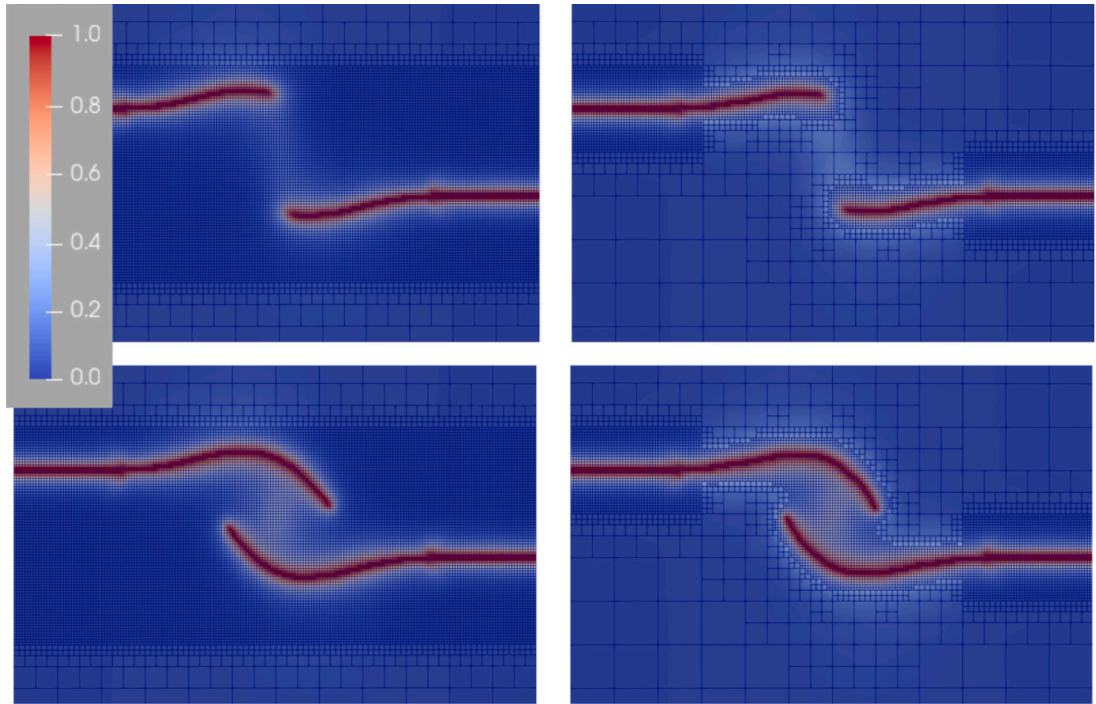


Fig. 28. Damage field on successive meshes for the AMR and cycle jump accelerated model.

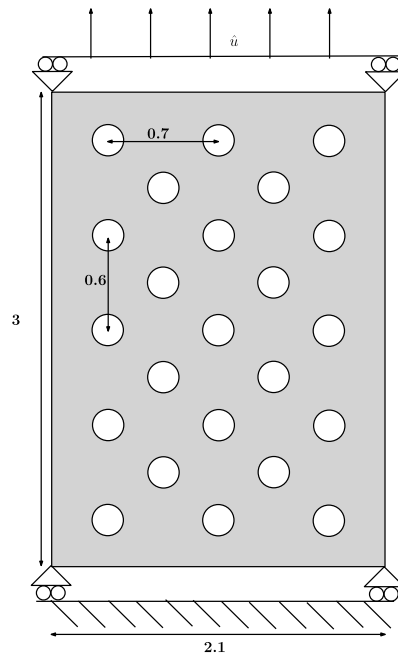


Fig. 29. Geometry in mm and boundary conditions.

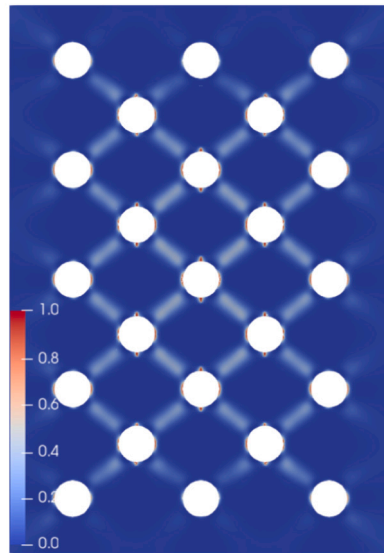


Fig. 30. Damage field after initiation.

discriminate between compressive and tensile loadings [64,65]. In Carrara et al. [14], a so-called “no tension” split [66], was used to model quasi brittle materials. As opposed to the spectral split, it enabled a good recovery of experimental data on this specific geometry: vertical cracks were observed, with no spurious damage in the compressive zones.

These results pointed at the fact that crack nucleation and crack growth were indeed recovered by the proposed algorithm, even in the presence of AMR and cycle jump schemes. Moreover, this sample highlighted the deficiencies of the spectral split, as well as the need for a relevant energy decomposition scheme to reproduce specific experimental results.

7. Conclusion

This work aimed at accelerating computations of high-cycle fatigue simulations with the most used fatigue extension of the phase-field model: a phenomenological approach based on Carrara et al. [14]. To achieve efficiency gains, time discretization was first optimized through the use of a cycle jump scheme that enabled extrapolation of large chunks of cycles during propagation. An iterative approach based on Loew et al. [25] was implemented to skip cycles while keeping a predefined accuracy. Then, space discretization was optimized through adaptive mesh refinement tools designed specifically for this phase-field formulation. With this tool, a relevant mesh was constructed during crack propagation to keep a low number of degrees of freedom while recovering a good approximation of the solution. Finally, a coupling between all the introduced tools was proposed.

The new algorithm enabled significant computing gains by skipping large numbers of cycles, while simultaneously refining the mesh adaptively. The influence of the numerical parameters on accuracy and efficiency was studied against multiple numerical benchmarks. Additionally, several 2D geometries were simulated to illustrate the flexibility of the implementation and its ability to recover crack branching, kinking, coalescence and even nucleation. For all these examples, expected crack paths were recovered with the coupled accelerating tools, while reaching an acceleration factor of up to 157 compared to cycle-by-cycle simulations on the computed cases (see Table 4). This factor is extremely case dependant, and a general expression for the acceleration factor of AMR, cycle jump and their coupling is hard to define. On the one hand, AMR seems to enable an acceleration factor that can reach half an order of magnitude, on the other hand, as specified in Loew et al. [25], the cycle jump approach enables larger computing gains as the total life increases. We can hence expect larger gains for real-life application of this acceleration approach. Finally, the Paris regime emerging from the used fatigue extension was used to fit the model on an experimental sample. Again, crack paths were predicted quantitatively, and the algorithm that was put forward enabled a significant acceleration of the process.

However, the current implementation could be improved further by adding an adaptive choice of ΔN in order to optimize the number of computed cycles. Furthermore, a 3D extension of this work is planned in order to accelerate the 3D computations. It should be noted that such an extension would not require additional numerical treatment. Finally, the proposed coupling could be used to investigate more complex fatigue phenomena, such as plastic effects and mean load effects, which could expand the applicability of the algorithm to realistic cases of fatigue crack initiation and propagation. In fact, recent works in Refs. [23,24], done on phase-field fatigue modeling, expand on the constitutive choices of the model in order to add those fatigue effects in a unified framework. Those extensions of the model would still allow the presented accelerating framework to reduce computing time, and would hence be an interesting perspective for future works.

CRedit authorship contribution statement

Adrien Jacon: Conceptualization, Methodology, Writing – original draft, Review & editing, Visualization, Investigation. **Benoit Prabel:** Investigation, Supervision, Conceptualization, Review & editing, Funding acquisition. **Gergely Molnár:** Investigation, Supervision, Conceptualization, Review & editing. **Joffrey Bluthé:** Supervision, Review & editing. **Anthony Gravouil:** Supervision, conceptualization, Review & editing.

Declaration of competing interest

The authors declare that they have no known competing financial interests or personal relationships that could have appeared to influence the work reported in this paper.

Data availability

Data will be made available on request

Acknowledgments

The authors thank the French Atomic Commission (CEA) for their financial support, along with support from the GEN2&3/SIMEX project and a CFR grant.

Appendix. Finite element discretization

The numerical solutions were found by writing the weak form of the mechanical problem (17a), (17b), (17c) and damage problem (20), (17e) in a finite element method setting. We therefore introduce the shape functions \mathbf{N} and gradient \mathbf{B} , associated with \mathbf{u} and d respectively, and approximate these fields as vectors of discrete nodal values in Voigt Notation:

$$\mathbf{u} = \mathbf{N}_u \cdot \mathbf{u} \quad , \quad \nabla \mathbf{u} = \mathbf{B}_u \cdot \mathbf{u} \quad , \quad (\text{A.1})$$

$$d = \mathbf{N}_d \cdot \mathbf{d} \quad , \quad \nabla d = \mathbf{B}_d \cdot \mathbf{d}. \quad (\text{A.2})$$

Mechanical problem.

A damaged influenced mechanical problem is first solved iteratively, as the energy decomposition (6) introduces non-linearity. We write the equilibrium (17a), (17b), (17c) in this discrete setting as:

$$\mathbf{R}_u = \mathbf{F}_{int} - \mathbf{F}_{ext} \quad , \quad (\text{A.3a})$$

$$= \int_{\Omega} \mathbf{B}_u^T \boldsymbol{\sigma} dV - \int_{\Omega} \mathbf{N}_u^T \mathbf{b} dV + \int_{\partial\Omega_t} \mathbf{N}_u^T \mathbf{t} dS, \quad (\text{A.3b})$$

where $\boldsymbol{\sigma}$ is the damaged stress vector in Voigt notation. Finding the solution at time step n is achieved with a Newton–Raphson algorithm implying iterations of index j . We gradually add corrections to the initial solution $\mathbf{u}_n = \mathbf{u}_{n-1} + \sum_j \delta \mathbf{u}_n^j$; here we decompose the total correction $\Delta \mathbf{u}_n^j = \sum_j \delta \mathbf{u}_n^j$. Using these symbols, we express that at each iteration j , a linearized form of Eq. (A.3) is solved:

$$\mathbf{K}_u^{j-1} \cdot \delta \mathbf{u}^j = -\mathbf{R}_u^{j-1}. \quad (\text{A.4})$$

With a tangent matrix for the mechanical problem expressed as:

$$\mathbf{K}_u^{j-1} = \int_{\Omega} \mathbf{B}_u^T \mathbf{C}^{j-1} \mathbf{B}_u dV, \quad (\text{A.5})$$

where \mathbf{C}^{j-1} corresponds to a damaged material's stiffness matrix whose computation is detailed in Ref. [26]. As \mathbf{C} is defined at the integration points of the finite element mesh, damage influences the material's stiffness through these supports. Consequently, at every mechanical computation step, nodal damage \mathbf{d} is interpolated at the integration points. Furthermore, the resulting damaged material's stiffness matrix \mathbf{C} is updated at each internal iterations j .

Phase-field damage problem.

In this weakly coupled finite element setting, the damage problem stays linear, with respect to \mathbf{d} such that at each time step n we solve:

$$\mathbf{K}_d \cdot \mathbf{d}_n = \int_{\Omega} \mathbf{N}_d^T 2H dV \quad , \quad (\text{A.6})$$

with a phase-field stiffness matrix at the time step n defined as:

$$\mathbf{K}_d = \int_{\Omega} \mathbf{N}_d^T \left(2H + \frac{G_F}{l_c} \right) \mathbf{N}_d + \mathbf{B}_d^T (G_F \cdot l_c) \mathbf{B}_d dV. \quad (\text{A.7})$$

Note that, as in the previous section, the coupling with the mechanical fields is done via quantities defined at the integration points.

References

- [1] A.A. Griffith, The phenomena of rupture and flow in solids, *Philos. Trans. R. Soc. Lond. Ser. A Math. Phys. Eng. Sci.* 221 (582–593) (1921) 163–198.
- [2] G.R. Irwin, The formation of equilibrium cracks during brittle fracture. General ideas and hypotheses. Axially-symmetric cracks, *J. Appl. Mech.* 24 (1957) 361–364.
- [3] P. Paris, F. Erdogan, A critical analysis of crack propagation laws, *J. Basic Eng.* 85 (4) (1963) 528–533.
- [4] G.A. Francfort, J.-J. Marigo, Revisiting brittle fracture as an energy minimization problem, *J. Mech. Phys. Solids* 46 (8) (1998) 1319–1342.
- [5] B. Bourdin, G.A. Francfort, J.-J. Marigo, Numerical experiments in revisited brittle fracture, *J. Mech. Phys. Solids* 48 (4) (2000) 797–826.
- [6] L. Ambrosio, V.M. Tortorelli, Approximation of functional depending on jumps by elliptic functional via t-convergence, *Comm. Pure Appl. Math.* 43 (8) (1990) 999–1036.
- [7] C. Miehe, M. Hofacker, F. Welschinger, A phase field model for rate-independent crack propagation: Robust algorithmic implementation based on operator splits, *Comput. Methods Appl. Mech. Engrg.* 199 (45–48) (2010) 2765–2778.
- [8] G. Molnár, A. Gravouil, 2D and 3D abaqus implementation of a robust staggered phase-field solution for modeling brittle fracture, *Finite Elem. Anal. Des.* 130 (2017) 27–38.
- [9] J.L. Boldrini, E.A.B. de Moraes, L.R. Chiarelli, F.G. Fumes, M.L. Bittencourt, A non-isothermal thermodynamically consistent phase field framework for structural damage and fatigue, *Comput. Methods Appl. Mech. Engrg.* 312 (2016) 395–427.
- [10] Y.-S. Lo, M.J. Borden, K. Ravi-Chandar, C.M. Landis, A phase-field model for fatigue crack growth, *J. Mech. Phys. Solids* 132 (2019) 103684.
- [11] G. Amendola, M. Fabrizio, Thermomechanics of damage and fatigue by a phase field model, *J. Therm. Stresses* 39 (2018).
- [12] P.J. Loew, B. Peters, L.A.A. Beex, Fatigue phase-field damage modeling of rubber using viscous dissipation: Crack nucleation and propagation, *Mech. Mater.* 142 (2020) 103282.
- [13] R. Alessi, S. Vidoli, L.D. Lorenzis, A phenomenological approach to fatigue with a variational phase-field model: The one-dimensional case, *Eng. Fract. Mech.* 190 (2018) 53–73.
- [14] P. Carrara, M. Ambati, R. Alessi, L.D. Lorenzis, A framework to model the fatigue behaviour of brittle materials on a variational phase-field approach, *Comput. Methods Appl. Mech. Engrg.* (2019).
- [15] M. Seiler, T. Linse, P. Hantschke, M. Kästner, An efficient phase-field model for fatigue fracture in ductile materials, *Eng. Fract. Mech.* 224 (2020) 106807.
- [16] J. Ulloa, J. Wambacq, R. Alessi, G. Degrande, S. François, Phase-field modeling of fatigue coupled to cyclic plasticity in an energetic formulation, *Comput. Methods Appl. Mech. Engrg.* 373 (2021).
- [17] K. Seleš, F. Aldakheel, Z. Tonković, J. Sorić, P. Wriggers, A phase-field model of thermo-elastic coupled brittle fracture with explicit time integration, *Comput. Mech.* 67 (2021) 1431–1452.
- [18] M. Simoes, C. Braithwaite, A. Makaya, E. Martínez-Pañeda, Modelling fatigue crack growth in shape memory alloys, *Fatigue Fract. Eng. Mater. Struct.* 45 (4) (2022) 1243–1257.
- [19] A. Golahmar, P.K. Kristensen, C.F. Niordson, E.M. nez Pañeda, A phase field model for hydrogen-assisted fatigue, *Int. J. Fatigue* 154 (2022).
- [20] A. Mesgarnejad, A. Imanian, A. Karma, Phase-field models for fatigue crack growth, *Theor. Appl. Fract. Mech.* 103 (2019) 102282.
- [21] M.M. Hasan, T. Baxevanis, A phase-field model for low-cycle fatigue of brittle materials, *Int. J. Fatigue* 150 (2021) 106297.
- [22] B.E. Grossman-Ponemon, A. Mesgarnejad, A. Karma, Phase-field modeling of continuous fatigue via toughness degradation, *Eng. Fract. Mech.* 264 (2022) 108255.
- [23] R. Alessi, J. Ulloa, Endowing griffith's fracture theory with the ability to describe fatigue cracks, 2023, Preprint submitted to Elsevier.
- [24] A. Golahmar, C.F. Niordson, E. Martínez-Pañeda, A phase field model for high-cycle fatigue: Total-life analysis, *Int. J. Fatigue* 170 (2023) 107558.
- [25] P.J. Loew, L.H. Poh, B. Peters, L.A.A. Beex, Accelerating fatigue simulations of a phase-field damage model for rubber, *Comput. Methods Appl. Mech. Engrg.* 370 (2020) 113247.
- [26] G. Molnár, A. Doitrand, A. Jacon, B. Prabel, A. Gravouil, Thermodynamically consistent linear-gradient damage model in Abaqus, *Eng. Fract. Mech.* 266 (2022) 108390.
- [27] J.-Y. Wu, V.P. Nguyen, A length scale insensitive phase-field damage model for brittle fracture, *J. Mech. Phys. Solids* 119 (2018) 20–42.
- [28] E. Tanné, T. Li, B. Bourdin, J.-J. Marigo, C. Maurini, Crack nucleation in variational phase-field models of brittle fracture, *J. Mech. Phys. Solids* 110 (2018) 80–99.
- [29] G. Molnár, A. Doitrand, R. Estevez, A. Gravouil, Toughness or strength? Regularization in phase-field fracture explained by the coupled criterion, *Theor. Appl. Fract. Mech.* 109 (2020) 102736.
- [30] P.K. Kristensen, C.F. Niordson, E. Martínez-Pañeda, An assessment of phase field fracture: Crack initiation and growth, *Phil. Trans. R. Soc. A* 379 (2203) (2021) 20210021.
- [31] P.-E. Bernard, N. Moës, N. Chevaugeon, Damage growth modeling using the thick level set (TLS) approach: Efficient discretization for quasi-static loadings, *Comput. Methods Appl. Mech. Engrg.* 233 (2012) 11–27.
- [32] CEA, Cast3M - finite element software developed by the French alternative energies and atomic energy commission, 2022, URL cast3m-m.cea.fr.
- [33] T. Helfer, B. Bary, T.T. Dang, O. Fandeur, B. Michel, Modélisation par champ de phase de la fissuration des matériaux fragiles: Aspects numériques et applications au combustible nucléaire oxyde, 13ème Colloque National en Calcul de Structure, 2017, CSMA 2017.
- [34] Y. Lu, T. Helfer, B. Bary, O. Fandeur, An efficient and robust staggered algorithm applied to the quasi-static description of brittle fracture by a phase-field approach, *Comput. Methods Appl. Mech. Engrg.* 370 (2020) 113218.
- [35] S. Riad, D. Bardel, J. Réthoré, Effect of microstructural length scales on crack propagation in elastic Cosserat media, *Eng. Fract. Mech.* 267 (2022) 108399.
- [36] G. Gibert, B. Prabel, A. Gravouil, C. Jacquemoud, A 3D automatic mesh refinement X-FEM approach for fatigue crack propagation, *Finite Elem. Anal. Des.* 157 (2019).
- [37] P.K. Kristensen, E. Martínez-Pañeda, Phase field fracture modelling using quasi-Newton methods and a new adaptive step scheme, *Theor. Appl. Fract. Mech.* 107 (2020) 102446.
- [38] D. Cojocaru, A. Karlsson, A simple numerical method of cycle jumps for cyclically loaded structures, *Int. J. Fatigue* 28 (12) (2006) 1677–1689.
- [39] J. Lemaitre, I. Doghri, Damage 90: A post processor for crack initiation, *Comput. Methods Appl. Mech. Engrg.* 115 (3–4) (1994) 197–232.
- [40] W.V. Paepegem, J. Degrieck, Fatigue degradation modelling of plain woven glass/epoxy composites, *Composites A* 32 (10) (2001) 1433–1441.
- [41] P.K. Kristensen, A. Golahmar, E. Martínez-Pañeda, C.F. Niordson, Accelerated high-cycle phase field fatigue predictions, *Eur. J. Mech. A Solids* 100 (2023) 104991.
- [42] J. Rannou, A. Gravouil, M.C. Baietto-Dubourg, A local multigrid X-FEM strategy for 3-D crack propagation, *Internat. J. Numer. Methods Engrg.* 77 (4) (2009) 581–600.
- [43] J.-C. Passieux, J. Réthoré, A. Gravouil, M.-C. Baietto, Local/global non-intrusive crack propagation simulation using a multigrid X-FEM solver, *Comput. Mech.* 52 (6) (2013) 1381–1393.
- [44] C. Miehe, F. Welschinger, M. Hofacker, Thermodynamically consistent phase-field models of fracture: Variational principles and multi-field FE implementations, *Internat. J. Numer. Methods Engrg.* 83 (10) (2010) 1273–1311.
- [45] B. Bourdin, G.A. Francfort, J.-J. Marigo, *The Variational Approach to Fracture*, Springer Netherlands, 2008.

- [46] T. Heister, M.F. Wheeler, T. Wick, A primal-dual active set method and predictor-corrector mesh adaptivity for computing fracture propagation using a phase-field approach, *Comput. Methods Appl. Mech. Engrg.* 290 (2015) 466–495.
- [47] H. Badnava, M.A. Msekh, E. Etemadi, T. Rabczuk, An h-adaptive thermo-mechanical phase field model for fracture, *Finite Elem. Anal. Des.* 138 (2018) 31–47.
- [48] S. Zhou, X. Zhuang, Adaptive phase field simulation of quasi-static crack propagation in rocks, *Undergr. Space* 3 (3) (2018) 190–205.
- [49] H.-Y. Kim, H.-G. Kim, A novel adaptive mesh refinement scheme for the simulation of phase-field fracture using trimmed hexahedral meshes, *Internat. J. Numer. Methods Engrg.* 122 (6) (2020) 1493–1512.
- [50] H. Hirshikesh, A.L.N. Pramod, H. Waisman, S. Natarajan, Adaptive phase field method using novel physics based refinement criteria, *Comput. Methods Appl. Mech. Engrg.* 383 (2021) 113874.
- [51] F. Freddi, L. Mingazzi, Mesh refinement procedures for the phase field approach to brittle fracture, *Comput. Methods Appl. Mech. Engrg.* 388 (2022) 114214.
- [52] T. Wick, Goal functional evaluations for phase-field fracture using PU-based DWR mesh adaptivity, *Comput. Mech.* 57 (6) (2016) 1017–1035.
- [53] K. Mang, M. Walloth, T. Wick, W. Wollner, Mesh adaptivity for quasi-static phase-field fractures based on a residual-type a posteriori error estimator, *GAMM-Mitt.* 43 (1) (2019).
- [54] H. Hirshikesh, C. Jansari, K. Krishna, R. Annabattula, S. Natarajan, Adaptive phase field method for quasi-static brittle fracture using a recovery based error indicator and quadtree decomposition, *Eng. Fract. Mech.* 220 (2019).
- [55] D. Perić, C. Hochard, M. Dutko, D.R.J. Owen, Transfer operators for evolving meshes in small strain elasto-plasticity, *Comput. Methods Appl. Mech. Engrg.* 137 (3–4) (1996) 331–344.
- [56] J. Mediavilla, R.H.J. Peerlings, M.G.D. Geers, A robust and consistent remeshing-transfer operator for ductile fracture simulations, *Comput. Struct.* 84 (8–9) (2006) 604–623.
- [57] M. Klinsmann, D. Rosato, M. Kamlah, R.-M. McMeeking, An assessment of the phase field formulation for crack growth, *Comput. Methods Appl. Mech. Engrg.* 294 (2015) 313–330.
- [58] G. Gibert, Propagation de Fissures En Fatigue Par Une Approche X-FEM Avec Raffinement Automatique de Maillage (Ph.D. thesis), INSA de Lyon, 2019.
- [59] M.-É. Schwaab, T. Biben, S. Santucci, A. Gravouil, L. Vanel, Interacting cracks obey a multiscale attractive to repulsive transition, *Phys. Rev. Lett.* 120 (25) (2018).
- [60] C. Schreiber, R. Müller, C. Kuhn, Phase field simulation of fatigue crack propagation under complex load situations, *Arch. Appl. Mech.* 91 (2) (2020) 563–577.
- [61] C.A. Tang, R.H.C. Wong, K.T. Chau, P. Lin, Modeling of compression-induced splitting failure in heterogeneous brittle porous solids, *Eng. Fract. Mech.* 72 (4) (2005) 597–615.
- [62] T.T. Nguyen, J. Yvonnet, Q.-Z. Zhu, M. Bornert, C. Chateau, A phase field method to simulate crack nucleation and propagation in strongly heterogeneous materials from direct imaging of their microstructure, *Eng. Fract. Mech.* 139 (2015) 18–39.
- [63] R. Romani, Rupture En Compression des Structures Hétérogènes à Base de Matériau Quasi-Fragiles (Ph.D. thesis), Université Pierre et Marie Curie, 2013.
- [64] Q.-C. He, Q. Shao, Closed-form coordinate-free decompositions of the two-dimensional strain and stress for modeling tension–compression dissymmetry, *J. Appl. Mech.* 86 (3) (2019).
- [65] M. Strobl, T. Seelig, On constitutive assumptions in phase field approaches to brittle fracture, *Procedia Struct. Integr.* 2 (2016) 3705–3712.
- [66] F. Freddi, G. Royer-Carfagni, Regularized variational theories of fracture: A unified approach, *J. Mech. Phys. Solids* 58 (8) (2010) 1154–1174.